A Theoretical Framework for Analyzing Coupled Neuronal Networks: Application to the Olfactory System

Andrea K. Barreiro [1], Shree Hari Gautam [2], Woodrow L. Shew [2], Cheng Ly [3*],

1 Department of Mathematics, Southern Methodist University, Dallas, TX 75275 U.S.A.
2 Department of Physics, University of Arkansas, Fayetteville, AR 72701 U.S.A.
3 Department of Statistical Sciences and Operations Research, Virginia Commonwealth University, Richmond, VA 23284 U.S.A.

* CLy@vcu.edu

Abstract

Determining how synaptic coupling within and between regions is modulated during sensory processing is an important topic in neuroscience. Electrophysiological recordings provide detailed spiking information about neurons but have traditionally been confined to a particular region or layer of cortex. Here, we develop a novel theoretical framework that relies on efficiently calculating the first and second order statistics in a multi-population firing rate model. We apply this method to determine qualitative relationships between important network connections in the rat olfactory system, when the model is constrained by data from simultaneous dual micro-electrode array *in vivo* recordings from two distinct regions, the olfactory bulb (**OB**) and anterior piriform cortex (**PC**). In particular, the model predicts that: i) inhibition within the afferent region (OB) has to be less than the inhibition in PC, ii) excitation from PC to OB is often stronger than excitation from OB to PC, iii) excitation from PC to OB and inhibition within PC have to both be relatively strong compared to presynaptic inputs from OB. These predictions are validated in a full spiking (leaky integrate-and-fire) neural network model of the OB–PC pathway that satisfies the many constraints from our experimental data. We find when the derived relationships are violated, the spiking statistics no longer satisfy the constraints from the data. In principle this modeling framework can be adapted to other systems and be used to investigate relationships between other neural attributes besides network connection strengths. Thus, this work can serve as a guide to further investigations into the relationships of various neural attributes within and across different regions during sensory processing.

Author Summary

Sensory processing is known to span multiple regions of the nervous system. However, electrophysiological recordings during sensory processing have traditionally been limited to a single region or brain layer. Recent advances in experimental techniques have enabled simultaneous recordings of multiple populations and across different regions. This new data allow us to pose the following question: what are the crucial neural network connections that enable sensory processing across different regions? Furthermore, how are these these connections interrelated?

We address this question by developing a novel theoretical framework to efficiently calculate spiking statistics in a multi-population firing rate model. These fast calculations enable exploration of a high-dimensional parameter space of possible networks, where we derive relationships between the effective network coupling strengths within and across regions. We apply this method to the olfactory system, by using simultaneous array recordings of the olfactory bulb and anterior piriform cortex to constrain the model. We are able to derive several relationships between the effective network coupling strengths within and across

these two regions. Our framework is adaptable to other systems and should be a valuable theoretical tool for investigating underlying neural features for sensory processing across regions.

Introduction

As experimental tools advance, measuring whole-brain dynamics with single-neuron resolution becomes closer to reality [2, 32, 36, 58]. However, a much harder task that remains technically elusive is to measure the interactions within and across brain regions that govern such system-wide dynamics. Here we develop a theoretical approach to elucidate such interactions based on easily-recorded properties such as mean and (co-)variance of firing rates in multiple regions and how they change at the onset of sensory stimulation. Although previous theoretical studies have addressed how spiking statistics depend on various mechanisms [8, 9, 19], these studies have typically been limited to a single region, leaving open the challenge of how inter-regional interactions impact the system dynamics, and ultimately the coding of sensory signals [3, 20, 34, 49, 72].

As a test case for our new theoretical tools, we studied interactions in the olfactory system. We used two micro-electrode arrays to simultaneously record from olfactory bulb (**OB**) and anterior piriform cortex (**PC**). Constrained by these experimental data, we developed computational models and theory to investigate interactions within and between OB and PC. The modeling framework includes two distinct regions: a network that receives direct sensory stimuli (here, the OB), and a second neural network (PC) that is reciprocally coupled to the afferent region. Each individual population is modeled via a firing rate model [71], but because of the two regions and our focus on correlated spiking, we still have a system of six (6) stochastic differential equations and thus a large-dimensional parameter space even in this minimal model. Analysis of this system would be unwieldy in general; we develop a novel method to compute firing statistics that is computationally efficient, captures the results of Monte Carlo simulations, and can provide analytic insight.

Thorough analysis of experimental data in both the spontaneous and stimulus-evoked states leads to a number of constraints on first- and second-order spiking statistics— many of which could not be observed using data from just one micro-electrode array. In particular, we find twelve (12) constraints that are consistent across different odorant stimuli. We use our theory/model to study an important subset of neural attributes (i.e., particular synaptic strengths) and investigate what relationships, if any, must be satisfied in order to robustly capture the many constraints observed in the data. We find that: i) inhibition within OB has to be less than the inhibition in PC, ii) excitation from PC to OB is often stronger than excitation from OB to PC, iii) excitation from PC to OB and inhibition within PC have to both be relatively strong compared to inputs originating in OB (inhibition from OB and excitation from OB to PC). We validate these guiding principles in a full spiking neural network (leaky integrate-and-fire **LIF**) model, mimicking the OB–PC pathway with synaptic delays, by showing that the many constraints from the experimental data are *all* satisfied. Finally, we demonstrate that violating these relationships in the LIF model results in spiking statistics that do not satisfy all of the data constraints.

Our predictions provide insights on interactions in the olfactory system that are difficult to directly measure experimentally. Importantly, these predictions were inferred from spike rates and variability, which are relatively easy to measure. We believe that the general approach we have developed – using easy-to-measure quantities to predict hard-to-measure interactions – will be valuable in diverse future investigations of how whole-brain function emerges from interactions among its constituent components.

Results

Our main result is the development of a theoretical framework to infer connection strengths (hard to measure) in a minimal firing rate model constrained by experimental data (commonly measured spike count statistics), validating the results in a full spiking neural network, withs a specific application to the olfactory system. The next paragraph summarizes the **Results** section exposition in the order of the presentation.

We performed simultaneous dual micro-electrode recordings with an array placed in the olfactory bulb (**OB**) and one placed in the anterior piriform cortex (**PC**) with the animal anesthetized and tracheotomized (see **Materials and Methods**). In this paper, we focus on the spike count statistics rather than the detailed temporal structure of the neural activity (Fig 1A–B). First we analyze the experimental data and compare the average (across cells or pairs) first and second order firing statistics, considering all combinations between spontaneous and evoked states and cell type (OB or PC). Then we present a minimal firing rate model where we develop a method to quickly and efficiently calculate the firing statistics in a coupled noisy neural network consisting of 6 neurons. As a test case for our methods and framework, we investigate the structure of four important parameters that result in firing statistics that satisfy all constraints from the experimental data. The results are then validated with a full spiking network of leaky integrate-and-fire (**LIF**) model neurons.

Consistent Trends in the Experimental Data

We first present our data from simultaneous dual micro-electrode array recordings, in which anesthetized rats were presented with odors. During each trial an odor was presented for roughly one second; recording continued for a total of 30 seconds. This sequence was repeated for 10 trials with 2-3 minutes in between trials; the protocol was repeated for another odor. Recordings were processed to extract single-unit activity; the number of units identified was: 23 in OB and 38 in PC (first recording, two odors), 18 in OB and 35 in PC (second recording, another two odors). In total, there were 4 different odors presented.

We divided each 30 s trial into two segments, representing the odor-**evoked** state (first 2 seconds) and the **spontaneous** state (remaining 28 seconds). We computed first- and second-order statistics for identified units; i.e. firing rate ν_k, spike count variance, and spike count covariance (we also computed two derived statistics, Fano Factor and Pearson's correlation coefficient, for each cell/cell pair). Spike count variances, covariances and correlations were computed using time windows T_{win} ranging between 5 ms and 2 s. In computing population statistics we distinguished between different odors (four total), different regions (OB vs. PC), and different activity states (spontaneous vs. evoked); otherwise, we assumed statistics were stationary over time.

We analyzed the data to identify relationships among these standard measures of spiking activity. We found twelve (12) robust relationships that held across multiple odorants. Table 1 summarizes the consistent relationships we found in our data, and Fig 1C–D, Fig 2, Fig 3 show the data exhibiting these relationships when combining all odorant stimuli (see S1 Text for statistics plotted by distinct odors). Throughout the paper, when comparing activity states the spontaneous state is in black and the evoked state in red; when comparing regions the OB cells/pairs are in blue and PC in green.

A common observation across different animals and sensory systems, is that firing rates increase in the evoked state (see, for example, Figure 3 in [14]). Indeed, we observed that average firing rates in both the OB and PC were higher in the evoked state than in the spontaneous state (Fig 1C–D). Furthermore, the firing rate in the OB was larger than the firing rate in the PC, in both spontaneous and evoked states (see mean values in Fig 1C–D).

Stimulus-induced decorrelation appears to be a widespread phenomena in many sensory systems and in many animals [19]; stimulus-induced decorrelation was previously reported in PC cells under different experimental conditions [48]. Here, we found that in the PC, the average spike count correlation is lower in the evoked state (red) than in the spontaneous state (black), at least for time windows of 0.5 s and above (Fig 2A). Although we show a range of T_{win} for completeness, we focus on the larger time windows because in our experiments the odors are held for 1 s and our subsequent methods only address long time-averaged spiking statistics. Note that we did not generally observe stimulus-induced decorrelation in the OB cells.

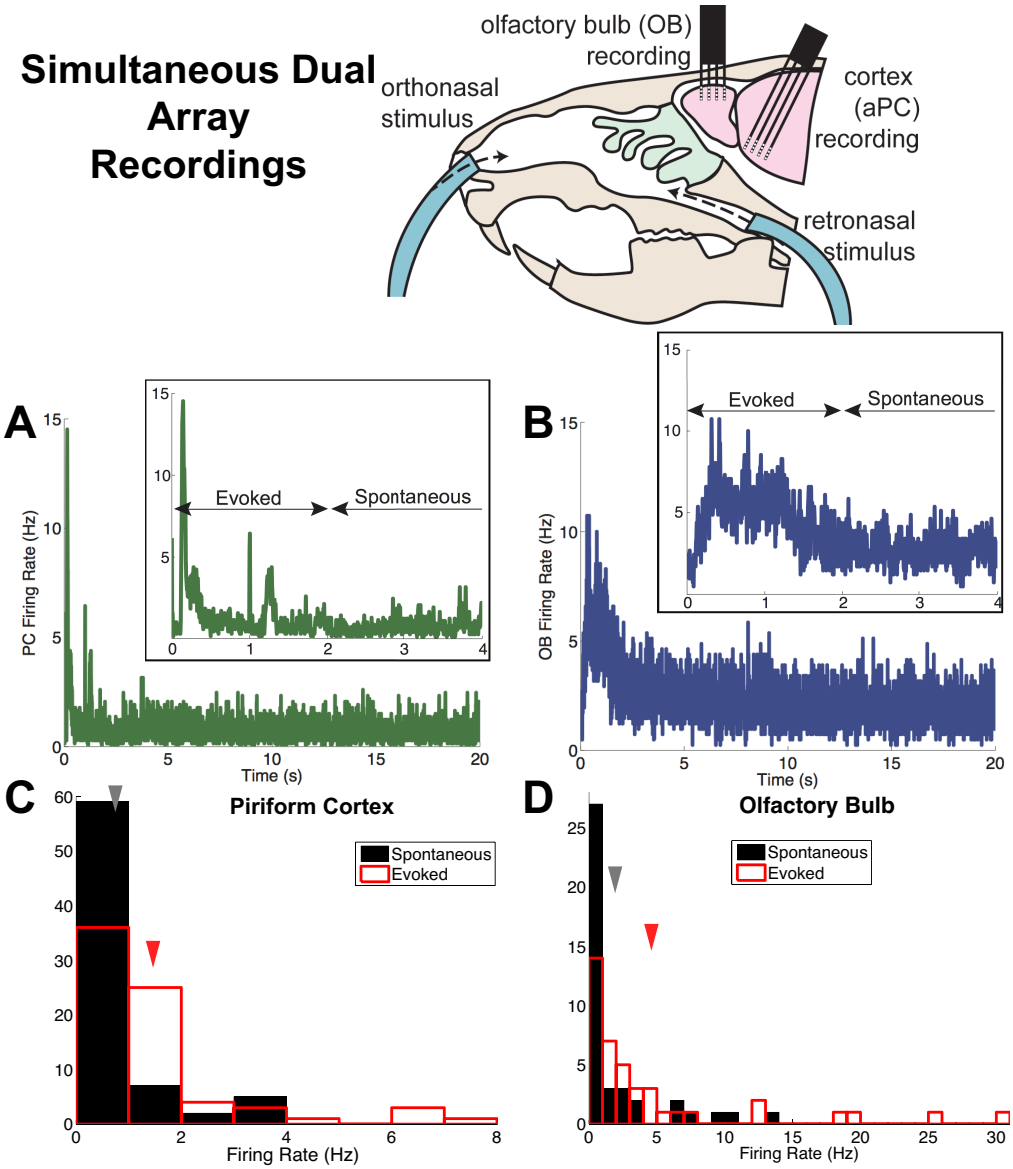

Fig 1. Population firing rates in anterior piriform cortex (PC) and olfactory bulb (OB) from simultaneous dual array recordings. (A) Trial-averaged population firing rate in time from 73 PC cells (38 and 35 cells from two recordings). The inset shows a closeup view, to highlight the distinction between spontaneous and evoked states. (B) Trial-averaged population firing rate in time from 41 OB cells (23 and 18 cells from two recordings). Inset as in (A); both (A) and (B) use 5 ms time bins. (C) The PC firing rate (averaged in time and over trials) of individual cells in the spontaneous (black) and evoked states (red). The arrows indicate the mean across 73 cells; the mean±std. dev. in the spontaneous state is: 0.75 ± 0.93 Hz, in the evoked state is: 1.5 ± 1.6 Hz. (D) Similar to (C), but for the OB cells described in (B). The mean±std. dev. in the spontaneous state is: 2 ± 3.3 Hz, in the evoked state is: 4.7 ± 7.1 Hz.

Another common observation in cortex, is for variability to decrease at the onset of stimulus [14]: in Fig 2B we see that the Fano Factor of spike counts in PC cells decreases in the evoked state (red) compared to the spontaneous state (black); note that other experimental labs have observed this decrease in the Fano

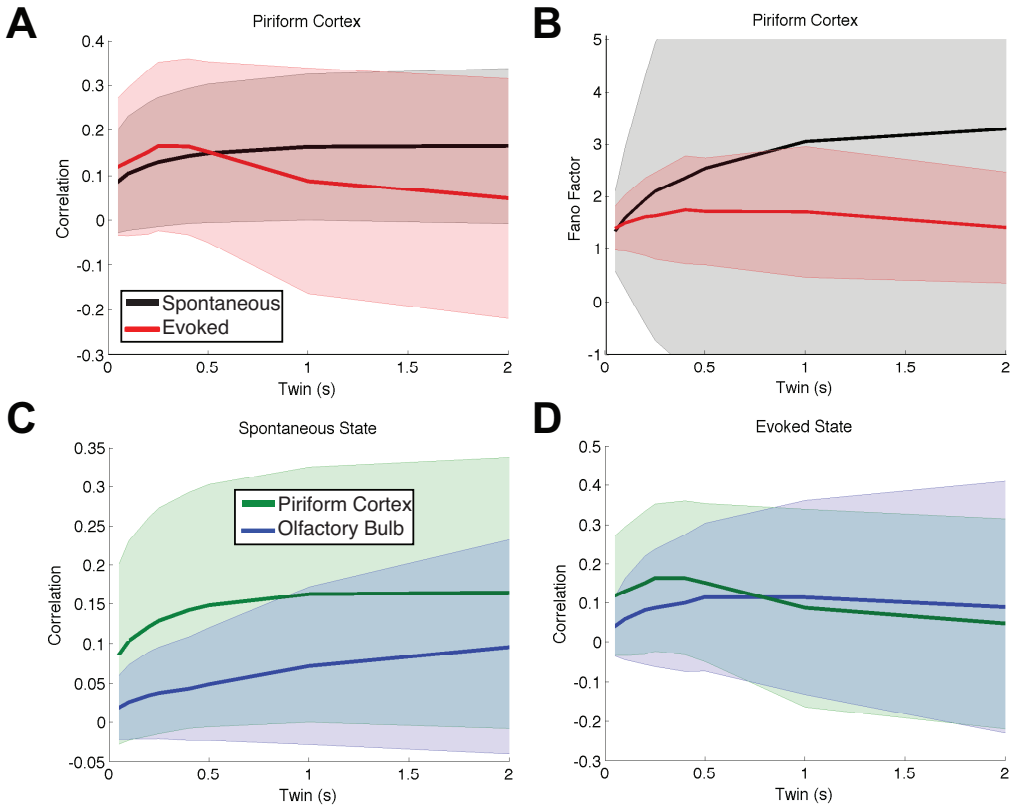

Fig 2. A subset of the important relationships between the spiking statistics in spontaneous and evoked states. Consistent trends that hold for *all* 4 odorant stimuli in the experimental data. Each panel shows two spike count statistics, as a function of the time window T_{win}. The shaded error bars denote 1 standard deviation (across all pairs or all cells) above and below the mean statistic. A: Stimulus-induced decorrelation of PC cell pairs (red) compared to the spontaneous state (black). B: The variability in PC (measured by Fano Factor) is lower in the evoked state (red) than in the spontaneous state (black). (C) In the spontaneous state, the average correlation of PC pairs (green) is *higher* than that of OB pairs (blue). (D) In the evoked state, the average correlation of PC pairs (green) is *lower* than that of OB pairs (blue). There were 406 total OB pairs and 1298 total PC pairs. (Although the trend is not apparent in (A) and (D) for smaller time windows, recall that the stimuli were held for 1 s and that our focus is on the larger time windows; smaller time windows are shown for completeness.)

factor of PC cells (see supplemental figure S6D in [48]). Fig 2C–D shows a comparison of PC and OB spike count correlation in the spontaneous state and evoked state, respectively. Spike count correlation in PC (green) is larger than correlation in OB (blue) in the spontaneous state, but in the evoked state the relationship switches, at least for $T_{win} > 0.5$ sec.

Fig 3 shows the four remaining constraints that are consistent for all odors and for all time windows. The Fano Factor in PC (green) is larger than in OB (blue), in the spontaneous state (Fig 3A); spike count variance in PC (green) is smaller than in OB (blue) in the evoked state (Fig 3B); spike count covariance in PC (green) is smaller than in OB (blue) in the evoked state (Fig 3C); and in OB the spike count variance in the evoked state (red) is larger than spontaneous (black, Fig 3D). Throughout the paper, we scale the spike count variance and covariance by T_{win} for ease of visualization; this does not affect the relative relationships we describe.

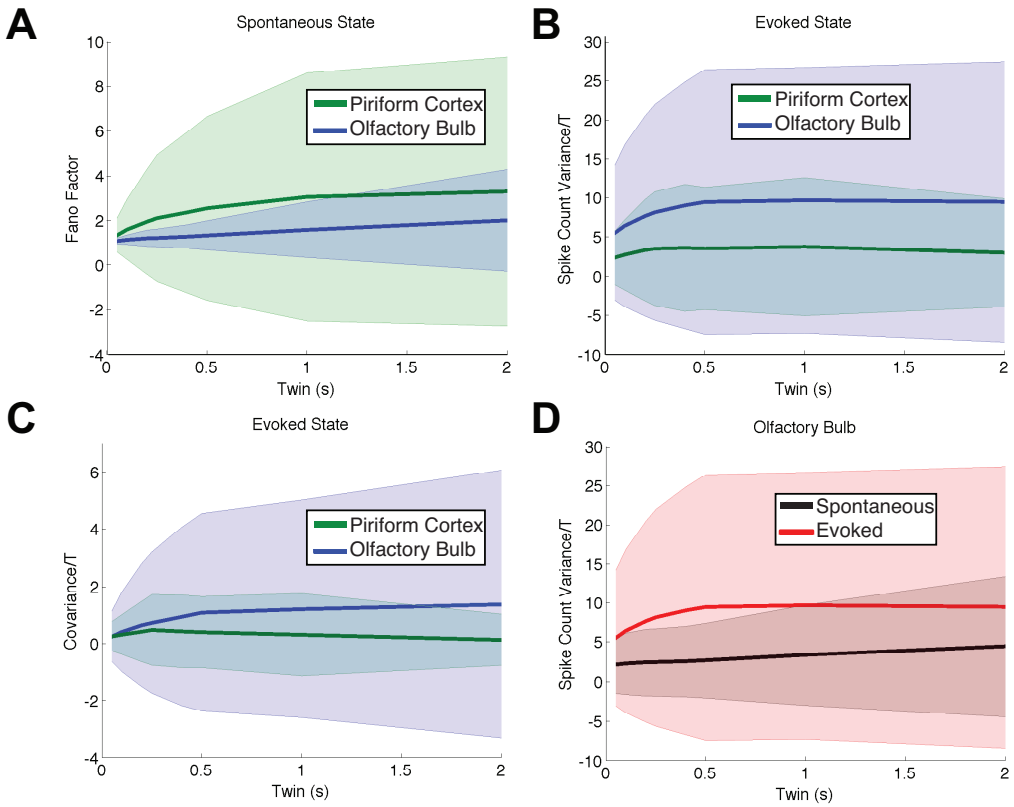

Fig 3. Showing the other trends from the experimental data that are consistent with all odors and for all time windows T_{win}. A: Fano Factor of spontaneous activity is larger in PC (green) than in OB (blue). B: The spike count variance in the evoked state is smaller in PC (green) than in OB (blue). C: Spike count covariance in the evoked state is smaller in PC (green) than in OB (blue). D: In OB cells, the evoked spike count variance (red) is larger than the spontaneous (black). The number of cells and number of pairs are the same as in Fig 2. Throughout we scale spike count variance and covariance by T_{win} for ease of visualization.

Table 1. The 12 relationships (constraints) that hold in the experimental data across all odors.

	Spont.	Evoked	Spon. to Evoked
Firing Rate	$\nu_{PC} < \nu_{OB}$	$\nu_{PC} < \nu_{OB}$	$\nu_{PC}^{Sp} < \nu_{PC}^{Ev}$
			$\nu_{OB}^{Sp} < \nu_{OB}^{Ev}$
Variability		$Var_{PC} < Var_{OB}$	$Var_{OB}^{Sp} < Var_{OB}^{Ev}$
	$FF_{PC} > FF_{OB}$		$FF_{PC}^{Sp} > FF_{PC}^{Ev}$
Co-variability		$Cov_{PC} < Cov_{OB}$	
	$\rho_{PC} > \rho_{OB}$	$\rho_{PC} < \rho_{OB}$	$\rho_{PC}^{Sp} > \rho_{PC}^{Ev}$

Relationships are of the averaged statistics across the population or all possible pairs that occurred with all odors. Other possible relationships were left out because they were ambiguous and/or odor dependent.

A Minimal Firing Rate Model to Capture Data Constraints

We model two distinct regions (OB and PC) with a system of six (6) stochastic differential equations, each representing the averaged activity of a neural population [71] or representative cell (see Fig 4 for a schematic of the network). For simplicity, in this section we use the word "cell" to refer to one of these populations. Each region has two excitatory (**E**) and one inhibitory (**I**) cell to account for a variety of spiking correlations [41]. We use $j \in \{1, 2, 3\}$ to denote three OB "cells" and $j \in \{4, 5, 6\}$ for three PC cells, with $j = 1$ as the inhibitory OB cell and $j = 4$ as the inhibitory PC cell. The equations are:

$$\tau \frac{dx_j}{dt} = -x_j + \mu_j + \sigma_j \eta_j + \sum_k g_{jk} F(x_k) \tag{1}$$

where $F(x_k)$ is a transfer function mapping activity to firing rate. Thus, the firing rate is:

$$\nu_j = F(x_j). \tag{2}$$

We set the transfer function to $F(X) = \frac{1}{2}\left(1 + \tanh((X - 0.5)/0.1)\right)$, a commonly used sigmoidal function [71] for all cells; experimental recordings of this function demonstrate it can be sigmoidal [13, 22, 57]. All cells receive noise η_j, the increment of a Weiner process, uncorrelated in time but correlated within a region: i.e. $\langle \eta_j(t) \rangle = 0$, $\langle \eta_j(t)\eta_j(t+s) \rangle = \delta(s)$, and $\langle \eta_j(t)\eta_k(t+s) \rangle = c_{jk}\delta(s)$. We set c_{jk} to:

$$c_{jk} = \begin{cases} 0, & \text{if } j \in \{1,2,3\}; k \in \{4,5,6\} \\ 1, & \text{if } j = k \\ c_{OB} & \text{if } j \neq k; j,k \in \{1,2,3\} \\ c_{PC} & \text{if } j \neq k; j,k \in \{4,5,6\} \end{cases} \tag{3}$$

The parameters μ_j and σ_j are constants that give the input mean and input standard deviation, respectively. Within a particular region (OB or PC), all three cells receive correlated background noisy input, but there is **no** correlated background input provided to both PC and OB cells. This is justified by the experimental data (see Fig S9); average pairwise OB-to-PC correlations are all relatively small, and in particular, less than pairwise correlations *within* the OB and PC. Furthermore, anatomically there are no known common inputs to both regions that are active at the same time.

We also set the background correlations to be higher in PC than in OB: i.e.

$$c_{PC} > c_{OB}.$$

This is justified in part in our array recordings where correlated local field potential fluctuations are larger in PC than in OB. Furthermore, one source of background correlation is global synchronous activity; Murakami et al. [50] has demonstrated that state changes (i.e., slow or fast waves as measured by EEG) strongly affect

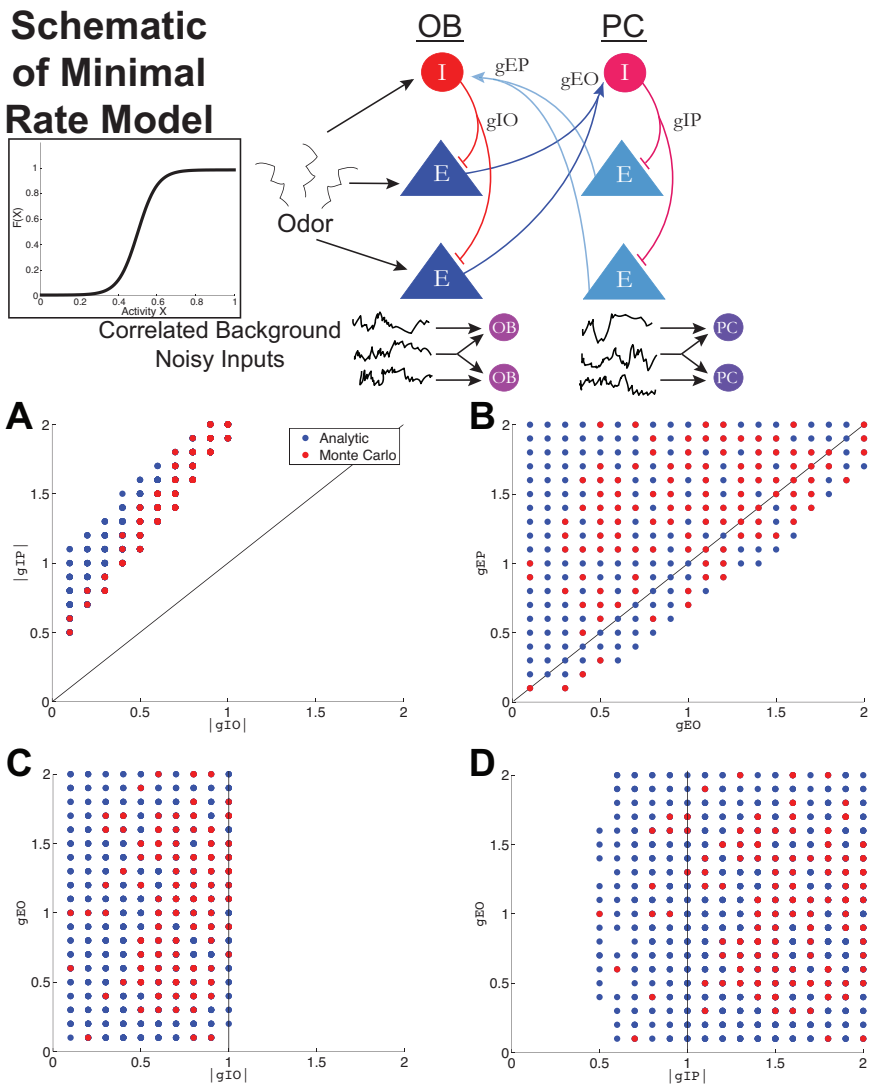

Fig 4. Minimal firing rate model to analyze important synaptic conductance strengths. A firing rate model (Wilson-Cowan) with background correlated noisy inputs is analyzed to derive principles relating these network attributes. This model only incorporates some of the anatomical connections that are known to exist *and* are important for modulation of statistics of firing (see main text for further discussion). Each neuron within a region (OB or PC) receives correlated background noisy input with $c_{OB} < c_{PC}$. Each plot shows parameter sets (4-tuples) that satisfy all 12 data constraints in Table 1, projected into a two-dimensional plane in parameter space. The blue dots show the result of the fast analytic method that satisfy all constraints; the red dots show the Monte Carlo simulations that satisfy all of the constraints. For computational purposes, we only tested the Monte Carlo on parameter sets that first satisfied the constraints in the fast analytic method. (A) The magnitude of the inhibition within PC ($|gIP|$) is greater than the magnitude of the inhibition within OB ($|gIO|$); all dots are above the diagonal line. (B) The excitation from PC to OB (gEP) is generally (but not always) larger than the excitation from OB to PC (gEO). (C) The inhibition within OB is generally weak; dots are to the left of the vertical line. (D) The inhibition within PC is generally strong; dots are to the right of the vertical line. Table 3 states the parameter values.

odorant responses in piriform cortex but only minimally effect olfactory bulb cells. Also, PC has more recurrent activity than the olfactory bulb; this could lead to more recurrent common input, if not cancelled

by inhibition [59].

We constructed our model to have two distinct activity states, spontaneous and evoked. We modeled the evoked state by increasing the three parameters μ_1, μ_2, μ_3, representing mean input to the olfactory bulb (values given in Table 3). All other parameters were the same for both states.

The model we have described may be less realistic than a large network of spiking models (such as Hodgkin-Huxley or leaky integrate-and-fire neurons). However, its simplicity permits fast and efficient evaluation of firing rate statistics, a necessity in exploring large parameter spaces that result in models satisfying numerous data constraints. Specifically, we calculate the statistics of the coupled network by solving a system of algebraic equations Eq 29–46 rather than using Monte Carlo simulations (see **Materials and Methods** for details). To derive tractable equations, we use an approximation based on asymptotic expansions. This allowed us to evaluate many parameter combinations, and therefore constrain the unknown coupling parameters, g_{jk}, which might otherwise be an intractable problem. Comparisons of the firing statistics computed from our method and Monte Carlo simulations show that the mean activity and firing rates are very accurate; variance and covariance (and thus correlation) are not as accurate, for larger coupling strengths (see Fig S10 in S2 Text comparing 100 random parameter sets). Nonetheless, we will find that the results are qualitatively replicated by more realistic spiking network models.

In principle, there can be up to 36 coupling strengths; however, we can make several assumptions:

- No cross-region inhibitory projections: $g_{41} = g_{51} = g_{61} = g_{14} = g_{24} = g_{34} = 0$.
- Excitatory $OB \to PC$ output will synapse only onto the inhibitory population: $g_{52} = g_{62} = g_{53} = g_{63} = 0$.
- Similarly, excitatory $PC \to OB$ output will synapse only onto the inhibitory population: $g_{25} = g_{26} = g_{35} = g_{36} = 0$.

Within OB, there is no excitatory (mitral cell) input to the inhibitory cells (i.e., granule cells), but feedforward inhibition is known to be a significant component in this circuit [12]. The OB to PC pathway has balanced excitation and inhibition [35]; however, within PC the recurrent activity is dominated by inhibition [35]. Previous work has also shown that inhibitory synaptic events are much more common in PC and are much easier to elicit [56]. Thus, the connection from excitatory OB to inhibitory PC (Fig 4) can thought of as the *net* effect of OB-to-PC connections. There is also experimental evidence that the feedback projections from PC to OB are dominated by inhibition [6, 44].

Even though several of the assumptions in this circuit are not anatomically correct (e.g., no E-to-E connections from OB to PC), we again emphasize that this is a *minimal* model meant to provide guiding principles about network structure and relative relationships, rather than precise anatomical modeling. Moreover, the next section will test the results on full spiking model with more realistic dynamics and features (containing these omitted connections).

We also made the following simplifying assumptions to limit the dimension of the parameter space of interest:

- Feedforward inhibitory connections within a population were identical: $gIO \equiv g_{21} = g_{31}$ and $gIP \equiv g_{54} = g_{64}$.
- Excitatory connections projecting outward from each region to the other region were identical: $gEO \equiv g_{42} = g_{43}$ and $gEP \equiv g_{15} = g_{16}$.
- No within-region excitatory connections; $g_{23} = g_{32} = g_{56} = g_{65} = 0$.

The resulting network model is illustrated in Fig 4.

Thus, we were left with four undetermined coupling strengths: gIO, gIP, gEO and gEP. We comprehensively surveyed a four-dimensional parameter space in which each coupling strength $|gIO|$, $|gIP|$, gEO, gEP was chosen between 0.1 and 2, with a interval of 0.1; giving us $20^4 = 1.6 \times 10^5$ total models. Given each choice of 4-tuple $\{gIO, gIP, gEO, gEP\}$, we computed first- and second-order statistics of both activity x_k and firing rates $F(x_k)$ using the formulas given in Eq (29)–(46), and checked the results satisfied the

constraints listed in Table 1. We found that approximately 1 % of all 4-tuples satisfied the constraints; we display them in Fig 4, by projecting all constraint-satisfying 4-tuples onto a two-dimensional plane where the axes are two of the four coupling parameters. We show four out of six possible pairs (the other two show qualitatively similar patterns, see Fig S11 in S2 Text): $|gIO|$ vs. $|gIP|$ (Fig 4A), gEO vs. gEP (Fig 4B), $|gIO|$ vs. gEP (Fig 4C), and $|gIP|$ vs. gEO (Fig 4D).

We found that:

- The magnitude of the inhibition within PC, $|gIP|$, is greater than the magnitude of the inhibition within OB, $|gIO|$ (Fig 4A: all dots are above the diagonal line).
- The excitation from PC to OB, gEP, is generally larger than the excitation from OB to PC, gEO.
- The inhibition within OB is generally weak (Fig 4C: dots are to the left of the vertical line).
- The inhibition within PC is generally strong (Fig 4D: dots are to the right of the vertical line).

The statistics computed in Eqs. 29–46 rely on the assumption that the activity distributions x_k are only weakly perturbed from a normal distribution; this may be violated for larger coupling strengths. Thus, we used Monte Carlo simulations of Eq 1 to check the accuracy of this approximation; specifically we performed Monte Carlo simulations on each 4-tuple of parameters for which the analytic approximation met our constraints. The resulting parameter set that satisfied all twelve (12) constraints are included as red dots in Fig 4A–D (therefore a red dot indicates that all 12 constraints were satisfied both for the analytic approximation AND for the Monte Carlo simulations). The result was a smaller set of parameters, but it is evident that the qualitative results derived from the fast analytic solver hold for the Monte Carlo simulations. Moreover, these results were robust to the choice of transfer function: in Fig. S12, we show that the same constraints are obtained when using a "square root" transfer function, rather than a sigmoid.

Admissible coupling strengths are characterized by a low-dimensional surface in parameter space

Another way to more succinctly examine the structure of the four neural attributes: gIO, gEO, gIP, gEP is to consider a matrix:

$$A(j,:) = [gIO(j),\ gEO(j),\ gIP(j),\ gEP(j)] \tag{4}$$

where the j^{th} row of A corresponds to a parameter set where all 12 constraints are satisfied in the Monte Carlo simulation. A standard singular value composition (SVD) of this matrix:

$$A = U\Sigma V'$$

shows that one dimension in the parameter space accounts for 77.2 % of the variance (all singular values) and is thus a reasonable entity to describe the structure of the valid gIO, gEO, gIP, gEP values. We scale the eigenvector from V (since the column space corresponds to our desired parameter space) corresponding to the largest singular value to get:

$$v = [gIO,\ gEO,\ gIP,\ gEP]' = [-8.5,\ 14.3,\ -20,\ 18.8]' \tag{5}$$

which indeed exhibits all of the aforementioned relationships. Thus, we have well-characterized the structure of these four parameters.

Results are Validated in a Spiking LIF Network

We then sought to reproduce these results in a general leaky integrate-and-fire (**LIF**) spiking neuron model of the coupled OB-PC system. Rather than try to model the exact underlying physiological details of the olfactory bulb or anterior piriform cortex, we aim instead to use a generic spiking model with conductance-based synaptic input that is at least the bases for many cortical models.

We set the four conductance strength values that are the focus of our analysis to:

$$\begin{aligned} gIO &= 7 \\ gEO &= 10 \\ gIP &= 20 \\ gEP &= 15; \end{aligned} \tag{6}$$

See Fig 5 or Eq 65–67 for exact definitions of gXY; these conductance strength values are dimensionless scale factors. These values were selected to satisfy the relationships derived from the analysis of the rate model (see Fig 4) and resemble the scaled vector from the SVD characterization in Eq 5. In contrast to the minimal firing rate model, here the conductance values are all necessarily positive; an inhibitory reversal potential is used to capture the hyperpolarization that occurs upon receiving synaptic input.

With the conductance strengths in Eq 6, and other standard parameter values (see Table 4) in a transparent LIF model of the OB–PC pathway, we were able to easily satisfy all 12 constraints: see Table 2 and Fig 5.

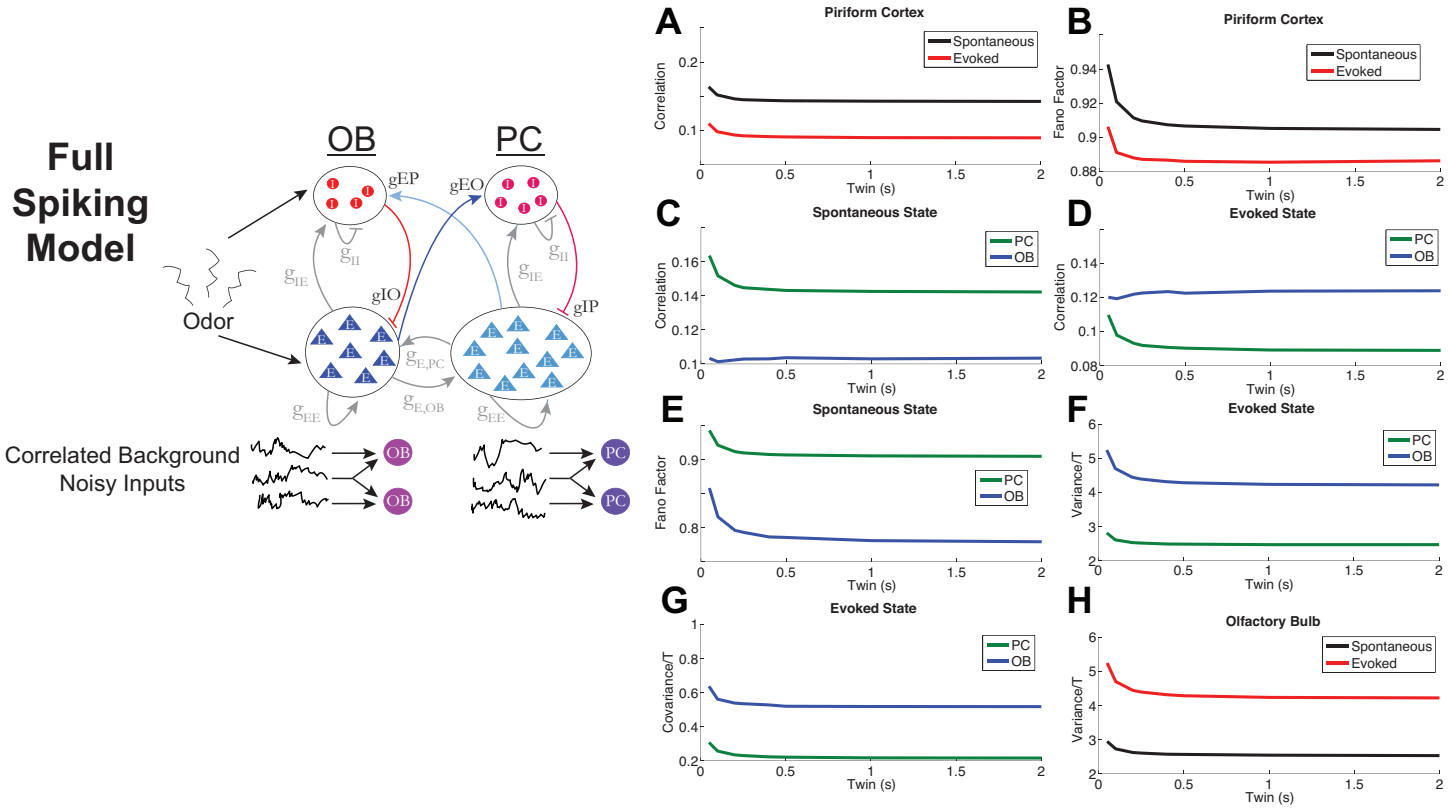

Fig 5. Detailed spiking LIF model confirms the results from analytic rate model. Schematic of the LIF model with 2 sets of recurrently coupled E and I cells. There are 12 types of synaptic connections. (A) Pairwise correlations in PC, spontaneous vs. evoked: $\rho^{Sp}_{PC} > \rho^{Ev}_{PC}$. (B) Variability (Fano factor) in PC, spontaneous vs evoked: $FF^{Sp}_{PC} > FF^{Ev}_{PC}$. (C) Correlations in the spontaneous state, PC vs. OB: $\rho^{Sp}_{PC} > \rho^{Sp}_{OB}$. (D) Correlations in the evoked state, PC vs. OB: $\rho^{Ev}_{PC} < \rho^{Ev}_{OB}$. (E) Variability (Fano factor) in the spontaneous state, PC vs. OB: $FF^{Sp}_{PC} > FF^{Sp}_{OB}$. (F) Variability (Fano factor) in the evoked state, PC vs. OB: $Var^{Ev}_{PC} < Var^{Ev}_{OB}$ in evoked state. (G) Covariances in the evoked state, PC vs. OB: $Cov^{Ev}_{PC} < Cov^{Ev}_{OB}$. (H) Variability (spike count variance) in OB, spontaneous vs. evoked: $Var^{Sp}_{OB} < Var^{Ev}_{OB}$. The curves show the average statistics over all $N_{OB/PC}$ cells or over all possible pairs $N_{OB/PC}(N_{OB/PC}-1)/2$. See **Materials and Methods** for model details, and Table 4 and Eq 6 for parameter values.

Table 2. Population firing rate statistics from an LIF model of the OB–PC pathway.

	Mean Firing Rate (Hz)	Std. Dev. (Hz)
ν_{OB}^{Sp}	3.8	3.3
ν_{OB}^{Ev}	8.5	5.6
ν_{PC}^{Sp}	2.1	2.5
ν_{PC}^{Ev}	4.2	7.3

See **Materials and Methods** for model details, and Table 4 and Eq 6 for parameter values. The mean and standard deviations are across the heterogeneous population.

While the firing rates in the LIF network (Table 2) do not *quantitatively* match with the firing rates from the experimental data, a few *qualitative* trends are apparent: (i) the ratio of mean spontaneous to evoked firing rates are similar to that observed in experimental data, for both OB and PC, (ii) the same is true of the standard deviation, (iii) the ratio of the mean OB firing rate to PC firing rate is similar to what is observed in the experimental data, in both spontaneous and evoked states. Therefore, the LIF network captures the mean firing rates reasonably well.

One significant difference between the LIF spiking network and the minimal firing rate model is that in the evoked state, mean background input to *both* the OB and PC cells is increased, compared to the spontaneous state (recall that in the minimal firing rate model, only the mean input to the OB cells increased in the evoked state; this insured that stimulus-induced changes in PC was due to network activity). When the mean input to the PC cells is the same in the spontaneous and evoked states, 11 of the 12 constraints were satisfied – the exception was the relative variability in PC between the spontaneous and evoked states, $FF_{PC}^{Sp} > FF_{PC}^{Ev}$ (see Fig. S13). The reason is that as firing rates increase, the OB spiking is more variable and thus the synaptic input from OB to PC is noisier, so the PC activity inherits this extra variability.

To capture this twelfth constraint, we allowed mean input drive to PC to increase in the evoked state. This has also been used in previous theoretical studies to achieve stimulus-induced decreases in spiking variability [38]. Other theoretical studies on stimulus-induced decreases in spiking variability had an extra source of variability in the spike generating mechanism (doubly stochastic process) which is simply removed with the stimulus [14]; our model only has one source of variability. Thus, the mechanism we employ to capture the Fano Factor constraint is reasonable and consistent with other studies on stimulus-induced changes in variability [14, 38].

Results of Violating Derived Relationships Between Conductance Strengths

What happens in the full LIF spiking network when the derived relationships between the conductance strengths are violated? Since the minimal firing rate model is very different quantitatively from the detailed spiking model, we do not expect the relationships between the conductance strengths to precisely hold. Not only are the underlying dynamics of the two models different, the number of cells, connections, as well as the number of parameters differ. Nevertheless, the minimal firing rate model is still useful in providing intuition in what would otherwise be a complicated network with a high-dimensional parameter space, where characterizing connection (conductance) strengths to satisfy the data constraints would be a msytery. We next demonstrate that when we violate the relationships derived in the previous section, a subset of the constraints in the experimental data (Table 1) will no longer be satisfied in the full spiking network.

The simulation time for a single parameter set in the full spiking model is time consuming (several days to to a week) because we are computing *all* covariance and correlation values for all possible pairs ($\mathcal{O}(N^2)$) in this completely heterogeneous network, for a variety of time windows, and the required number of realizations for accurate spiking statistics is large. Thus, we cannot exhaustively explore the parameter space; recall that the purpose of the method we developed in the minimal firing rate model is for faster computation. Instead, we distill results into three tests:

1. Make $gIO > gIP$ by setting $gIO = 20$ and $gIP = 7$.

2. Make $gEO > gEP$ by setting $gEO = 15$ and $gEP = 1$

3. Make gEP and gIP relatively smaller by setting $gEP = 10$ and $gIP = 10$

The original values (used in Fig 5) for these parameters were given in Eq 6.

The result of Test 1 is that 7 of the 12 constraints are violated (see Fig S14 in S2 Text); most importantly stimulus-induced decorrelation of the PC cells, which is particularly important in the context of coding, was not present. In addition, the PC firing rates are larger than the OB firing rates in both states, the evoked PC correlation is larger than evoked OB correlation, the spontaneous PC Fano Factor is larger than spontaneous OB Fano Factor, and both the variance and covariance of PC is larger than OB in the evoked state (all of which violate the constraints from our data).

The result of Test 3 is that 4 of the 12 constraints are violated (see Fig S16 in S2 Text), including again stimulus-induced decorrelation of the PC cells. The evoked PC correlation is larger than evoked OB correlation, and both the variance and covariance of PC are larger than the corresponding quantities in OB in the evoked state. Both these two tests (1 and 3) indicate that these two qualitative relationships (stronger effective inhibition within PC and stronger effective presynaptic inputs from PC) are robust with respect to both the detailed LIF spiking model and the minimal firing rate model.

The result of Test 2 is not as straightforward as the others. We did not exhaustively search parameter space due to the vast computational resources this would require, but in several parameter sets with $gEO > gEP$, we found the resulting network statistics could still satisfy all of the constraints (e.g., with $gEO = 15$ and $gEP = 1$, as well as with $gEO = 20$ and $gEP = 1$). The reason for this may be that in the two coupled recurrent networks we chose very different gIO and gIP values to begin with (7 and 20, respectively), and would thus require gEO and gEP to be significantly different to counter-balance this. Also, notice in the minimal firing rate model results in Fig 4B that there are a significant number of red dots below the diagonal, indicating that the relationship $gEP > gEO$ does not have to strictly hold. However, we did find a condition where this test demonstrates the value of the minimal firing rate model; we changed $\tilde{c}_{OB}$ from 0.5 to 0.6 (recall $\tilde{c}_{PC} = 0.8$). (Note that in the minimal firing model that $c_{OB} = 0.3$ and $c_{PC} = 0.35$, relatively close in value.) The result of Test 2 ($gEO = 15$ and $gEP = 1$) with $\tilde{c}_{OB} = 0.6$ is that one constraint is violated: ρ^{Sp}_{PC} is no longer less than ρ^{Sp}_{OB} (see Fig S15 in S2 Text). This suggests that the relationship that $gEO > gEP$ is not as robust as the others and can be violated.

In summary, the intuitions gained from the results and analysis of the minimal firing rate model are generally transferable to a more complex spiking model of the OB–PC pathway, but may require further investigations and perhaps experiments for validation.

Discussion

As electrophysiological recording technology advances, there will be more datasets with simultaneous recordings of neurons spanning larger regions of the nervous system. Such networks are inherently high-dimensional, making mechanistic analyses generally intractable without fast and reasonably accurate approximation methods. We have developed a computational reduction method for a multi-population firing rate model [71] that enables analysis of the spiking statistics. Our work specifically enables theoretical characterizations of an important, yet hard-to-measure quantity, connection strength, using easy-to-measure spiking statistics. The method is computationally efficient, is validated with Monte Carlo simulations of spiking neural networks, and can provide analytic insight.

Our computational methods are applied to simultaneous dual-array recordings in two distinct regions of the olfactory system: the olfactory bulb (OB) and anterior piriform cortex (PC). Our unique experimental dataset enables a detailed analysis of the first- and second-order spike count statistics in two activity states, and a comparison of how these statistics are related between OB and PC cells. We found twelve (12) consistent trends across four odors in the dataset (Table 1), and sought to identify what neural network attributes would account for these trends. We focused on four important network attributes, specifically the conductance strengths in the following connections: feedforward inhibition within OB, within PC, excitatory projections from OB to inhibitory PC neurons, and finally excitatory projections from PC to OB inhibitory neurons

(granule cells). Our reduced firing rate model predicts several relationships that are then verified with a more detailed spiking network model, specifically: i) inhibition within the OB has to be less than the inhibition in PC, ii) excitation from PC to OB is often stronger than excitation from OB to PC, iii) connections that originate within PC have to relatively strong compared to connections that originate within OB. These results make a strong prediction that to the best of our knowledge is unknown and might be testable with simultaneous patch-clamp recordings.

In principle our theory could be used to study the structure of other network features such as background correlation, noise level, transfer function, etc.. It is straightforward mathematically to incorporate other desired neural attributes (with the caveat of perhaps increasing the overall number of equations and terms in the approximations) without changing the essence of the framework. Here we have focused on the role of the strength of synaptic coupling; however theoretical studies have shown that other neural attributes can effect spike statistics (in particular, spike count correlation) [15, 19], and some of these attributes can conceivably change with stimuli. Spike count correlations can depend on intrinsic neural properties [1, 4, 5, 29, 43, 53], network architecture [38, 60, 62] and synaptic inputs [37, 39, 41, 46, 59, 66] (or combinations of these [40, 55, 68]), plasticity [61], as well as top-down mechanisms [16, 47, 64]. Thus, correlation modulation is a rich and deep field of study, and we do not presume our result is the only plausible explanation for spike statistics modulation.

Although the minimal firing rate model did not include certain anatomical connections that are known to exist (e.g. recurrent excitation in the PC), the model is meant for deriving qualitative principles rather than precise quantitative modeling of the pathway. We based our simplifications on insights from recent experimental work: recent slice physiology work has shown that within PC, recurrent activity is dominated by inhibition [35]; previous work has also shown that inhibitory synaptic events are much more common (than excitatory synaptic events) in PC and are much easier to elicit [56]. Thus, the connection from excitatory OB cells to inhibitory PC cells (gEO in Fig 4) can thought of as the net effect of these connections along the lateral olfactory tract. Other theoretical analyses of effective feedforward inhibitory networks have also neglected anatomical E-to-E connections [41, 46]. Furthermore, this minimal model was validated with a more realistic, recurrently coupled spiking network, which did include within-region excitatory connections (see Fig 5 and Fig S14–S16 in S2 Text).

In computing statistics for the minimal firing rate model, we only considered asynchronous behavior, in which a set of stationary statistics can be solved self-consistently. More sophisticated methods might be used to address oscillatory dynamics (see [52] in which the adaptive quadratic integrate-and-fire model was successfully analyzed with a reduced method); capturing the firing statistics in these other regimes is a potentially interesting direction of research. The limitation to asynchronous statistics is not unique, but is shared by other approximation methods. Some methods are known to have issues when the system bifurcates [10, 11] because truncation methods can fail [42]. Several authors have proposed procedures to approximate the first- and second-order spiking statistics with equations derived by using truncations of moment expansions [10, 11, 31], or by perturbing from the large population size limit [7, 21]. These approaches generally approximate the dynamics of the entire network configuration based on a master equation, whereas we do not use a master equation or derive population-averaged dynamics from first principles. Instead, we focused here on perturbing from a background state in which several populations (each population modeled by a single equation) receive correlated background input but are otherwise uncoupled. This allows us to narrow our focus to how spike count co-variability from common input is modulated by recurrent connections.

In other related work, Paninski and colleagues [67] derived approximations to the firing statistics of generalized linear models [70] by assuming the net input is normally distributed. Although there are similarities in the underlying assumptions, they rely on large network size (and/or small input strengths) to appeal to the central limit theorem whereas the models here are exactly normally distributed without coupling.

We have only focused on first- and second-order firing statistics, even though other higher order statistics may be important [30, 54, 69] (but also see [65]). If downstream neurons use a linear decoding scheme, then first- and second-order spiking statistics are sufficient in quantitative measures of neural coding [18, 33]. It is currently unknown whether downstream neurons decode olfactory signals with a nonlinear decoder, but there

is evidence in other sensory systems that second order statistics are sufficient [34]. Recent work has shown that at the level of the olfactory bulb, decoding an odor in the presence of other odors might be more efficient using nonlinear decoding [27] (however see [45] who showed that linear decoding is plausible). Considering higher order spiking statistics may be an area of future research.

As a test case for our method, we use recordings from the olfactory system. The absence of breathing in tracheotomized rats in these experiments is only an approximation to olfactory processing in awake animals. However, there are benefits to tracheotomized animals: the complex temporal firing patterns are removed, making averaging over time to calculate spike count statistics less confounding because the firing statistics are closer to stationarity. In principle, we can incorporate breathing dynamics into our framework by including an oscillatory forcing term in Eq 1; this will be the subject of future work. While time-varying statistics are likely important in the olfactory bulb, there is evidence that in the anterior piriform cortex, spike count — rather than the timing — is most consequential for odor discrimination [48]. However, other studies have reported that timing of the stimuli in the olfactory bulb is important: [17,27,28] showed decoding performance is best at the onset of odors in mammals and worsens as time proceeds, whereas [23] found that decoding performance improved with time in zebrafish. These important issues are beyond the scope of this current study.

Materials and Methods

Electrophysiological Recordings

Subjects. All procedures were carried out in accordance with the recommendations in the Guide for the Care and Use of Laboratory Animals of the National Institutes of Health and approved by University of Arkansas Institutional Animal Care and Use Committee (protocol #14049). Experimental data was obtained from one adult male rat (289 g ; *Rattus Norvegicus*, Sprague-Dawley outbred, Harlan Laboratories, TX, USA) housed in an environment of controlled humidity (60%) and temperature (23°C) with 12 h light-dark cycles. The experiments were performed in the light phase.

Anesthesia. Anesthesia was induced with isoflurane inhalation and maintained with urethane (1.5 g/kg body weight (**bw**) dissolved in saline, intraperitoneal injection (**ip**)). Dexamethasone (2 mg/kg bw, ip) and atropine sulphate (0.4 mg/kg bw, ip) were administered before performing surgical procedures.

Double tracheotomy surgery. To facilitate ortho- and retronasal delivery of the odorants a double tracheotomy surgery was performed as described previously [26]. This allowed for the rat to sniff artificially while breathing naturally through the trachea bypassing the nose. A Teflon tube (OD 2.1 mm, upper tracheotomy tube) was inserted 10 mm into the nasopharynx through the rostral end of the tracheal cut. Another Teflon tube (OD 2.3 mm, lower tracheotomy tube) was inserted in to the caudal end of the tracheal cut to allow breathing. Both tubes were fixed and sealed to the tissues using surgical thread. Local anesthetic (2% Lidocaine) was applied at all pressure points and incisions. Throughout the surgery and electrophysiological recordings rats' core body temperature was maintained at 37°C with a thermostatically controlled heating pad.

Craniotomy surgery. Subsequently, a craniotomy surgery was performed on the dorsal surface of the skull at two locations, one over the right Olfactory Bulb (2 mm × 2 mm, centered 8.5 mm rostral to bregma and 1.5 mm lateral from midline) and the other over the right anterior Pyriform Cortex (2 mm × 2 mm, centered 1.5 mm caudal to bregma and 5.5 mm lateral from midline).

Presentation of ortho- and retronasal odorants. The bidirectional artificial sniffing paradigm previously used for the presentation of ortho- and retronasal odorants [26] were slightly modified such that instead of a nose mask a Teflon tube was inserted into the right nostril and the left nostril was sealed by suturing. The upper tracheotomy tube inserted into the nasopharynx was used to deliver odor stimuli retronasally (Fig 1. We used two different odorants, Hexanal (**Hexa**) and Ethyl Butyrate (**EB**) by both ortho- and retronasal

routes, there by constituting 4 different odor stimuli. Each trial consisted of 10 one-second pulse presentations of an odor with 30 second interval in between two pulses, and 2-3 min in between two trials.

Electrophysiology. Extracellular voltage was recorded simultaneously from OB and aPC using two different sets of 32-channel microelectrode arrays (**MEAs**). (OB: A4x2tet, 4 shanks x 2 iridium tetrodes per shank, inserted 400 μm deep from dorsal surface; aPC: Buzsaki 32L, 4 shanks x 8 iridium electrode sites per shank, 6.5 mm deep from dorsal surface; NeuroNexus, MI, USA). Voltages were measured with respect to an AgCl ground pellet placed in the saline-soaked gel foams covering the exposed brain surface around the inserted MEAs. Voltages were digitized with 30 kHz sample rate as described previously [25] using Cereplex + Cerebus, Blackrock Microsystems (UT, USA).

Recordings were filtered between 300 and 3000 Hz and semiautomatic spike sorting was performed using Klustakwik software, which is optimized for the types of electode arrays used here [63]. After automatic sorting, each unit was visually inspected to ensure quality of sorting.

Data processing

After the array recordings were spike sorted to identify activity from distinct cells, we further processed the data as follows:

- We computed average firing rate for each cell, where the average was taken over all trials and over the entire trial length (i.e. not distinguishing between spontaneous and evoked periods); units with firing rates below 0.008 Hz and above 49 Hz were excluded.
- When spike times from the same unit were within 0.1 ms of each other, only the first (smaller) of the spike time was used and the subsequent spike times were discarded

We divided each 30 s trial into two segments, representing the odor-**evoked** state (first 2 seconds) and the **spontaneous** state (remaining 28 seconds). In each state, we are interested in the random spike counts of the population in a particular window of size T_{win}. For a particular time window, the j^{th} neuron has a spike count instance N_j in the time interval $[t, t + T_{win})$:

$$N_j = \sum_k \int_t^{t+T_{win}} \delta(t - t_k)\, dt \tag{7}$$

The spike count correlation between cells j and k is given by:

$$\rho_T = \frac{Cov(N_j, N_k)}{\sqrt{Var(N_j)Var(N_k)}}, \tag{8}$$

where the *covariance* of spike counts is:

$$Cov(N_j, N_k) = \frac{1}{n-1} \sum \left(N_j - \mu(N_j)\right)\left(N_k - \mu(N_k)\right). \tag{9}$$

Here n is the total number of observations of N_j, and $\mu(N_j) := \frac{1}{n}\sum N_j$ is the mean spike count across T_{win}-windows and trials. The correlation ρ_T is a normalized measure of the the trial-to-trial variability (i.e., noise correlation), satisfying $\rho_T \in [-1, 1]$; it is also referred to as the *Pearson's correlation coefficient*. For each cell pair, the covariance $Cov(N_j, N_k)$ and variance $Var(N_j)$ are empirically calculated by averaging across different time windows within a trial *and* different trials.

A standard measure of variability is the Fano Factor of spike counts, which is the variance scaled by the mean:

$$FF_k = \frac{Var(N_k)}{\mu(N_k)}. \tag{10}$$

In principle, any of the statistics defined here might depend on the time t as well as time window size T_{win}; here, we assume that Var, Cov, FF, and ρ_T are stationary in time, and thus separate time windows based only on whether they occur in the evoked (first 2 seconds) or spontaneous (last 28 seconds) state.

Each trial of experimental data has many time windows[1]; the exact number depends on the state, the value of T_{win}, and whether disjoint or overlapping windows are used. In this paper we use overlapping windows by half the length of T_{win}[2] to calculate the spiking statistics. The results are qualitatively similar for disjoint windows and importantly the relationships/constraints are the same with disjoint windows. We limit the size of $T_{win} \leq 2\,\mathrm{s}$ because this is the maximum duration of the evoked state, within each trial.

The average spike count $\mu(N_j)$ of the j^{th} neuron with a particular time window T_{win} is closely related the average firing rate of that neuron:

$$\nu_j := \frac{\mu(N_j)}{T_{win}} \tag{11}$$

Firing Rate Model

Recall that the activity in each representative cell is modeled by:

$$\tau \frac{dx_j}{dt} = -x_j + \mu_j + \sigma_j \eta_j + \sum_k g_{jk} F(x_k) \tag{12}$$

where $F(x_k)$ is a transfer function mapping activity to firing rate. Thus, the firing rate is:

$$\nu_j = F(x_j). \tag{13}$$

The index of each region is denoted as follows: $j \in \{1, 2, 3\}$ for the 3 OB cells, and $j \in \{4, 5, 6\}$ for the 3 PC cells, with $j = 1$ as the inhibitory OB cell and $j = 4$ as the inhibitory PC cell (see Fig 4). In this paper, we set $\sigma_1 = \sigma_2 = \sigma_3 = \sigma_{OB}$ and $\sigma_4 = \sigma_5 = \sigma_6 = \sigma_{PC}$ (see Table 3).

Table 3. Parameters of the rate model Eq 1. The only difference between the spontaneous and evoked states, is that the mean input to OB increased in the evoked state

	Parameter	Definition	Spontaneous Value	Evoked Value
Olfactory Bulb	μ_1	Mean Input	13/60	**26/60**
	μ_2		9/60	**18/60**
	μ_3		7/60	**14/60**
	σ_{OB}	Background Noise Level	1.4	1.4
	c_{OB}	OB Background Correlation	0.3	0.3
Piriform Cortex	μ_4	Mean Input	9/60	9/60
	μ_5		5/60	5/60
	μ_6		3/60	3/60
	σ_{PC}	Background Noise Level	2	2
	c_{PC}	PC Background Correlation	0.35	0.35

In the absence of coupling, any pair of activity variables, (x_j, x_k), are bivariate normally distributed because the equations:

$$\tau \frac{dx_j}{dt} = -x_j + \mu_j + \sigma_j \left(\sqrt{1 - c_{jk}} \xi_j(t) + \sqrt{c_{jk}} \xi_c(t) \right) \tag{14}$$

$$\tau \frac{dx_k}{dt} = -x_k + \mu_k + \sigma_k \left(\sqrt{1 - c_{jk}} \xi_k(t) + \sqrt{c_{jk}} \xi_c(t) \right) \tag{15}$$

[1] an exception is when $T_{win} = 2\,\mathrm{s}$; in the evoked state, there is only 1 window per trial

[2] e.g. if the trial length is 2 s and $T_{win} = 1\,\mathrm{s}$, then there are 3 total windows per trial: [0 s, 1 s], [0.5 s, 1.5 s], and [1 s, 2 s]

describes a multi-dimensional Ornstein-Uhlenbeck process [24]. Note that we have re-written $\eta_{j/k}(t)$ as sums of independent white noise processes $\xi(t)$, which is always possible for Gaussian white noise. Since $x_j(t) = \frac{1}{\tau}\int_0^t e^{-(t-u)/\tau}\Big[\mu_j + \sigma_j\eta_j(u)\Big]\,du$, we calculate marginal statistics as follows:

$$\mu(j) \equiv \langle x_j\rangle = \mu_j + 0 \tag{16}$$

$$\begin{aligned}
\sigma^2(j) &\equiv \langle (x_j - \mu(j))^2\rangle \\
&= \left\langle \frac{\sigma_j^2}{\tau^2}\int_0^t\int_0^t e^{-(t-u)/\tau}\eta_j(u)e^{-(t-v)/\tau}\eta_j(v)\,du\,dv\right\rangle \\
&= \frac{\sigma_j^2}{\tau^2}\lim_{t\to\infty}\int_0^t e^{-2(t-u)/\tau}\,du = \frac{\sigma_j^2}{2\tau}
\end{aligned}$$

A similar calculations shows in general we have:

$$Cov(j,k) = \frac{c_{jk}}{2\tau}\sigma_j\sigma_k \tag{17}$$

Thus, $(x_j, x_k) \sim \mathcal{N}\left(\left(\begin{smallmatrix}\mu_j\\ \mu_k\end{smallmatrix}\right), \frac{1}{2\tau}\left(\begin{smallmatrix}\sigma_j^2 & \sigma_j\sigma_k c_{jk}\\ \sigma_j\sigma_k c_{jk} & \sigma_k^2\end{smallmatrix}\right)\right)$.
To simplify notation, let use define:

$$\rho_{SN}(y) := \frac{1}{\sqrt{2\pi}}e^{-y^2/2}, \text{ the standard normal PDF} \tag{18}$$

$$\rho_{2D}(y_1,y_2) := \frac{1}{2\pi\sqrt{1-c_{jk}^2}}\exp\Big(-\frac{1}{2}\vec{y}^T\left(\begin{smallmatrix}1 & c_{jk}\\ c_{jk} & 1\end{smallmatrix}\right)^{-1}\vec{y}\Big), \text{ bivariate standard normal} \tag{19}$$

With coupling, an exact expression for a joint distribution for $(x_1, x_2, x_3, x_4, x_5, x_6)$ is not explicitly known. However, we can estimate this distribution (and any derived statistics, such as means and variances) using Monte Carlo simulations. All Monte Carlo simulations of the six (6) coupled SDEs were performed using a time step of 0.01 (we set $\tau = 1$) with a standard Euler-Maruyama method, for a time of 5000 units (arbitrary, but relative to the characteristic time scale $\tau = 1$) for each of the 3000 realizations. The activity x_j was sampled at each time step after an equilibration period.

Furthermore, we can approximate moments of the joint distribution under the assumption of weak coupling, described in the next section.

Approximation of Firing Statistics in the Firing Rate Model

We will now show how to compute approximate first and second order statistics for the firing rate model with coupling; i.e. we aim to compute the mean activity $\langle x_j\rangle$, mean firing rate $\langle F(x_j)\rangle$, variance and covariances of both: $\langle x_j x_k\rangle$ and $\langle F(x_j)F(x_k)\rangle$. For a simpler exposition, we have only included eight synaptic connections; we have excluded autaptic connections, E→E connections, and E→I connections within a region.

An equation for each statistic can be calculated by first writing Eq (12) as a low-pass filter of the right-hand-side:

$$x_j(t) = \frac{1}{\tau}\int_0^t e^{-(t-u)/\tau}\Big[\mu_j + \sigma_j\eta_j(u) + \sum_k g_{jk}F(x_k)\Big]\,du \tag{20}$$

We then take expectations, letting $t\to\infty$; e.g.

$$\mu(j) := \langle x_j\rangle = \mu_j + \langle\sum_k g_{jk}F(x_k)\rangle = \mu_j + \sum_k g_{jk}\langle F(x_k)\rangle \tag{21}$$

If the stochastic process is ergodic — generally true for stochastic differential equations of this type — then averaging over time is equivalent to averaging over the invariant measure.

We will make several assumptions for tractability. First, we only account for direct connections in the formulas for the first and second order statistics, assuming the terms from the indirect connections are either small or already accounted for in the direct connections. We further make the following assumptions to simplify the calculations:

$$\left\langle \int_0^t F(x_k(u))e^{-(t-u)/\tau}\,du \int_0^t F(x_k(v))e^{-(t-v)/\tau}\,dv \right\rangle \approx \frac{\tau}{2}\mathbb{E}\left[F^2(x_k)\right] \tag{22}$$

$$\text{where } \mathbb{E}\left[F^2(x_k)\right] := \int F^2(\sigma(k)y+\mu(k))\,\rho_{SN}(y)\,dy \tag{23}$$

$$\left\langle \int_0^t \sigma_j\eta_j(u)e^{-(t-u)/\tau}\,du \int_0^t F(x_k(v))e^{-(t-v)/\tau}\,dv \right\rangle \approx \frac{\tau}{2}\mathbb{E}\left[N_jF(x_k)\right],\ \text{if } j\neq k \tag{24}$$

$$\text{where } \mathbb{E}\left[N_jF(x_k)\right] := \frac{\sigma_j}{\sqrt{2}}\iint y_1F(\sigma(k)y_2+\mu(k))\,\rho_{2D}(y_1,y_2)\,dy_1dy_2 \tag{25}$$

$$\left\langle \int_0^t \sigma_j\eta_j(u)e^{-(t-u)/\tau}\,du \int_0^t F(x_k(v))e^{-(t-v)/\tau}\,dv \right\rangle$$
$$\approx \frac{\tau}{2}\frac{\sigma_k}{\sqrt{2}}\int yF(\sigma(k)y+\mu(k))\,\rho_{SN}(y)\,dy,\ \text{if } j=k \tag{26}$$

$$\left\langle \int_0^t F(x_j(u))e^{-(t-u)/\tau}\,du \int_0^t F(x_k(v))e^{-(t-v)/\tau}\,dv \right\rangle \approx \frac{\tau}{2}\mathbb{E}\left[F(x_j)F(x_k)\right] \tag{27}$$

$$\text{where } \mathbb{E}\left[F(x_j)F(x_k)\right] :=$$
$$\iint F(\sigma(j)y_1+\mu(j))F(\sigma(k)y_2+\mu(k))\,\rho_{2D}(y_1,y_2)\,dy_1dy_2 \tag{28}$$

and N_j denotes the random variable $\int_0^t \sigma_j\eta_j(u)e^{-(t-u)/\tau}\,du$, which is by itself normally distributed with mean 0 and variance $\sigma_j^2\tau/2$.

Each assumption is equivalent to the assumption that two of the random variables of interest are δ-correlated in time; thus avoiding the need to compute autocorrelation functions explicitly. The first assumption, Eq 22, states that $F(x_j(t))$ is δ-correlated with itself; the second and third, Eq 24 and Eq 26, address N_j and $F(x_k(t))$, for $j\neq k$ and $j=k$ respectively. Finally, the fourth assumption, Eq 27, states that $F(x_j(t))$ and $F(x_k(t))$ are δ-correlated.

In all of the definitions for the expected values with ρ_{2D}, note that the underlying correlation correlation c_{jk} depend on the pair of interest (j,k). Finally, we assume that the activity variables (x_j,x_k) are pairwise normally distributed with the subsequent statistics; this is sufficient to "close" our model and solve for the statistical quantities self-consistently. This last assumption is implicitly a weak coupling assumption because with no coupling, (x_j,x_k) are bivariate normal random variables.

The resulting approximations for the mean activity are:

$$\mu(1) = \mu_1 + g_{15}\int F(\sigma(5)y + \mu(5))\,\rho_{SN}(y)\,dy + g_{16}\int F(\sigma(6)y + \mu(6))\,\rho_{SN}(y)\,dy \tag{29}$$

$$\mu(2) = \mu_2 + g_{21}\int F(\sigma(1)y + \mu(1))\,\rho_{SN}(y)\,dy \tag{30}$$

$$\mu(3) = \mu_3 + g_{31}\int F(\sigma(1)y + \mu(1))\,\rho_{SN}(y)\,dy \tag{31}$$

$$\mu(4) = \mu_4 + g_{42}\int F(\sigma(2)y + \mu(2))\,\rho_{SN}(y)\,dy + g_{43}\int F(\sigma(3)y + \mu(3))\,\rho_{SN}(y)\,dy \tag{32}$$

$$\mu(5) = \mu_5 + g_{54}\int F(\sigma(4)y + \mu(4))\,\rho_{SN}(y)\,dy \tag{33}$$

$$\mu(6) = \mu_6 + g_{64}\int F(\sigma(4)y + \mu(4))\,\rho_{SN}(y)\,dy. \tag{34}$$

The resulting approximation to the variances of the mean activity are:

$$\begin{aligned}
\tau\sigma^2(1) &= \frac{\sigma_1^2}{2} + \frac{g_{15}^2}{2}Var\big(F(\sigma(5)Y + \mu(5))\big) + \frac{g_{16}^2}{2}Var\big(F(\sigma(6)Y + \mu(6))\big) \\
&\quad + g_{15}g_{16}Cov\big(F(\sigma(5)Y_1 + \mu(5)), F(\sigma(6)Y_2 + \mu(6))\big)
\end{aligned} \tag{35}$$

$$\begin{aligned}
\tau\sigma^2(2) &= \frac{\sigma_2^2}{2} + \frac{g_{21}^2}{2}Var\big(F(\sigma(1)Y + \mu(1))\big) \\
&\quad + \sigma_2 g_{21}\iint \frac{y_1}{\sqrt{2}}F(\sigma(1)y_2 + \mu(1))\,\rho_{2D}(y_1, y_2)\,dy_1 dy_2
\end{aligned} \tag{36}$$

$$\begin{aligned}
\tau\sigma^2(3) &= \frac{\sigma_3^2}{2} + \frac{g_{31}^2}{2}Var\big(F(\sigma(1)Y + \mu(1))\big) \\
&\quad + \sigma_3 g_{31}\iint \frac{y_1}{\sqrt{2}}F(\sigma(1)y_2 + \mu(1))\,\rho_{2D}(y_1, y_2)\,dy_1 dy_2
\end{aligned} \tag{37}$$

$$\begin{aligned}
\tau\sigma^2(4) &= \frac{\sigma_4^2}{2} + \frac{g_{42}^2}{2}Var\big(F(\sigma(2)Y + \mu(2))\big) + \frac{g_{43}^2}{2}Var\big(F(\sigma(3)Y + \mu(3))\big) \\
&\quad + g_{42}g_{43}Cov\big(F(\sigma(2)Y_1 + \mu(2)), F(\sigma(3)Y_2 + \mu(3))\big)
\end{aligned} \tag{38}$$

$$\begin{aligned}
\tau\sigma^2(5) &= \frac{\sigma_5^2}{2} + \frac{g_{54}^2}{2}Var\big(F(\sigma(4)Y + \mu(4))\big) \\
&\quad + \sigma_5 g_{54}\iint \frac{y_1}{\sqrt{2}}F(\sigma(4)y_2 + \mu(4))\,\rho_{2D}(y_1, y_2)\,dy_1 dy_2
\end{aligned} \tag{39}$$

$$\begin{aligned}
\tau\sigma^2(6) &= \frac{\sigma_6^2}{2} + \frac{g_{64}^2}{2}Var\big(F(\sigma(4)Y + \mu(4))\big) \\
&\quad + \sigma_6 g_{64}\iint \frac{y_1}{\sqrt{2}}F(\sigma(4)y_2 + \mu(4))\,\rho_{2D}(y_1, y_2)\,dy_1 dy_2
\end{aligned} \tag{40}$$

In Eq 29–40, all of the Var and Cov are with respect to $Y \sim \mathcal{N}(0,1)$ (for Var) and $(Y_1, Y_2) \sim \mathcal{N}\left(\binom{0}{0}, \frac{1}{2}\begin{pmatrix} 1 & c_{jk} \\ c_{jk} & 1 \end{pmatrix}\right)$ (for Cov); both are easy to calculate. The value c_{jk} depends on the pairs; for example in Eq 36, the ρ_{2D} has $c_{jk} = c_{ob}$, the background correlation value in the olfactory bulb but in Eq 35, the Cov term is with respect to ρ_{2D} with $c_{jk} = c_{pc}$, the background correlation value in the piriform cortex.

Lastly, we state the formulas for the approximations to the covariances. Although there are 15 total covariance values, we are only concerned with 6 covariance values (3 within OB and 3 within PC); we neglect all covariances *between* regions. First, our experimental data set shows that these covariance (and correlation) values are small (see Fig S9 in S2 Text). Second, because there is no background correlation (i.e common input) between PC and OB in our model, any nonzero covariance/correlation arises strictly via direct coupling.

Thus, we cannot view OB-PC covariance from coupling as a small perturbation of the background (uncoupled) state; we do not expect our model to yield qualitatively accurate predictions for these statistics. The formulas are:

$$\tau Cov(1,2) = \frac{1}{2}c_{ob}\sigma_1\sigma_2 + \sigma_1\frac{g_{21}}{2}\int \frac{y}{\sqrt{2}}F(\sigma(1)y+\mu(1))\,\rho_{SN}(y)\,dy \tag{41}$$

$$\tau Cov(1,3) = \frac{1}{2}c_{ob}\sigma_1\sigma_3 + \sigma_1\frac{g_{31}}{2}\int \frac{y}{\sqrt{2}}F(\sigma(1)y+\mu(1))\,\rho_{SN}(y)\,dy \tag{42}$$

$$\begin{aligned}\tau Cov(2,3) &= \frac{1}{2}c_{ob}\sigma_2\sigma_3 + \frac{g_{21}g_{31}}{2}Var\big(F(\sigma(1)Y+\mu(1))\big) \\ &\quad + \frac{\sigma_3 g_{21}+\sigma_2 g_{31}}{2}\iint \frac{y_1}{\sqrt{2}}F(\sigma(1)y_2+\mu(1))\,\rho_{2D}(y_1,y_2)\,dy_1dy_2\end{aligned} \tag{43}$$

$$\tau Cov(4,5) = \frac{1}{2}c_{pc}\sigma_4\sigma_5 + \sigma_4\frac{g_{54}}{2}\int \frac{y}{\sqrt{2}}F(\sigma(4)y+\mu(4))\,\rho_{SN}(y)\,dy \tag{44}$$

$$\tau Cov(4,6) = \frac{1}{2}c_{pc}\sigma_4\sigma_6 + \sigma_4\frac{g_{64}}{2}\int \frac{y}{\sqrt{2}}F(\sigma(4)y+\mu(4))\,\rho_{SN}(y)\,dy \tag{45}$$

$$\begin{aligned}\tau Cov(5,6) &= \frac{1}{2}c_{pc}\sigma_5\sigma_6 + \frac{g_{54}g_{64}}{2}Var\big(F(\sigma(4)Y+\mu(4))\big) \\ &\quad + \frac{\sigma_6 g_{54}+\sigma_5 g_{64}}{2}\iint \frac{y_1}{\sqrt{2}}F(\sigma(4)y_2+\mu(4))\,\rho_{2D}(y_1,y_2)\,dy_1dy_2\end{aligned} \tag{46}$$

Iteration procedure to solve for the approximate statistics self-consistently

Based on the approximations and resulting equations described in the previous section, our objective is to solve for the statistics of x_j self-consistently. Once these are determined, the statistics of the firing rates $F(x_j)$ are approximated with the same pairwise normal assumption on (x_j, x_k) (we are **not** assuming that $(F(x_j), F(x_k))$ are bivariate normal random variables).

We use a simple iterative procedure to solve the system of coupled algebraic expression for the statistics of x_j. We first solve the system in the absence of coupling (i.e. Eqn. (16), (17)), and use these values to start the iteration; at each step, the formulas for the means (29)–(34), variances (35)–(40), and covariances (41)–(46) are recalculated numerically, using the results of the previous step. The iteration stops once all 18 statistical quantities of the activity match up to a relative tolerance of 10^{-6} (convergence), or after 50 total iterations (non-convergence). The result with a given parameter set can either be: i) convergence, ii) non-convergence, iii) a pair of statistics with invalid covariance (non-positive definite covariance matrix), which is checked after i) and ii). We only consider parameter sets where the iteration has converged and all of the covariances are valid, after which we determine whether the constraints are satisfied.

One subtle point is that we did not use any of the numerically calculated Cov values in the bivariate normal distributions ρ_{2D}; rather, the correlation value is always c_{jk} which is either 0, c_{ob}, or c_{pc} depending on the pair. In principle, one can use a fully iterative procedure where the formulas for the Cov (41)–(46) are used in ρ_{2D}; however, we found that the resulting covariance matrices (for ρ_{2D}) can fail to be positive semi-definite. Handling this case requires additional code in the program and slower calculations for each parameter set, which is antithetical to the purpose of our method. We checked some parameter sets comparing the results of the two procedures, and the results are quantitatively similar.

The standard normal ρ_{SN} and bivariate ρ_{2D} PDFs have state variable(s) $y_{1,2}$ discretized from -3 to 3 with a mesh size of 0.01; integrals in Eqn. (29)–(46) are computed using the trapezoidal rule.

Simplified network with four coupling parameters

To further simplify the network, we:

- set $\tau = 1$,

- assume feedforward inhibitory connections within a region have the same strength; i.e. $g_{21} = g_{31} \equiv gIO$ and $g_{54} = g_{64} \equiv gIP$,
- assume cross-region excitatory connections are equal from the presynaptic cell, i.e., $g_{15} = g_{16} = gEP$ and $g_{42} = g_{43} = gEO$.
- assume $\sigma_1 = \sigma_2 = \sigma_3 =: \sigma_{ob}$ and $\sigma_4 = \sigma_5 = \sigma_6 =: \sigma_{pc}$

Now there are only 4 coupling parameters: gIO, gEO, gIP, gEP.

The above formulas for the statistics of x_j reduce to:

$$\mu(1) = \mu_1 + gEP \int \Big(F(\sigma(5)y + \mu(5)) + F(\sigma(6)y + \mu(6)) \Big) \rho_{SN}(y)\, dy \tag{47}$$

$$\mu(2) = \mu_2 + gIO \int F(\sigma(1)y + \mu(1))\, \rho_{SN}(y)\, dy \tag{48}$$

$$\mu(3) = \mu_3 + gIO \int F(\sigma(1)y + \mu(1))\, \rho_{SN}(y)\, dy \tag{49}$$

$$\mu(4) = \mu_4 + gEO \int \Big(F(\sigma(2)y + \mu(2)) + F(\sigma(3)y + \mu(3)) \Big) \rho_{SN}(y)\, dy \tag{50}$$

$$\mu(5) = \mu_5 + gIP \int F(\sigma(4)y + \mu(4))\, \rho_{SN}(y)\, dy \tag{51}$$

$$\mu(6) = \mu_6 + gIP \int F(\sigma(4)y + \mu(4))\, \rho_{SN}(y)\, dy; \tag{52}$$

the variances are:

$$\sigma^2(1) = \frac{\sigma_{ob}^2}{2} + \frac{g_{EP}^2}{2} Var\Big(F(\sigma(5)Y_1 + \mu(5)) + F(\sigma(6)Y_2 + \mu(6)) \Big) \tag{53}$$

$$\sigma^2(2) = \frac{\sigma_{ob}^2}{2} + \frac{g_{IO}^2}{2} Var\big(F(\sigma(1)Y + \mu(1)) \big) + \sigma_{ob} gIO \iint \frac{y_1}{\sqrt{2}} F(\sigma(1)y_2 + \mu(1))\, \rho_{2D}(y_1, y_2)\, dy_1 dy_2 \tag{54}$$

$$\sigma^2(3) = \sigma^2(2) \tag{55}$$

$$\sigma^2(4) = \frac{\sigma_{pc}^2}{2} + \frac{g_{EO}^2}{2} Var\Big(F(\sigma(2)Y_1 + \mu(2)) + F(\sigma(3)Y_2 + \mu(3)) \Big) \tag{56}$$

$$\sigma^2(5) = \frac{\sigma_{pc}^2}{2} + \frac{g_{IP}^2}{2} Var\big(F(\sigma(4)Y + \mu(4)) \big) + \sigma_{pc} gIP \iint \frac{y_1}{\sqrt{2}} F(\sigma(4)y_2 + \mu(4))\, \rho_{2D}(y_1, y_2)\, dy_1 dy_2 \tag{57}$$

$$\sigma^2(6) = \sigma^2(5); \tag{58}$$

the covariances are:

$$
\begin{aligned}
Cov(1,2) &= \frac{1}{2}c_{ob}\sigma_{ob}^2 + \sigma_{ob}\frac{gIO}{2}\int \frac{y}{\sqrt{2}}F(\sigma(1)y+\mu(1))\,\rho_{SN}(y)\,dy && (59)\\
Cov(1,3) &= Cov(1,2) && (60)\\
Cov(2,3) &= \frac{1}{2}c_{ob}\sigma_{ob}^2 + \frac{g_{IO}^2}{2}Var\big(F(\sigma(1)Y+\mu(1))\big) \\
&\quad +\sigma_{ob}gIO\iint \frac{y_1}{\sqrt{2}}F(\sigma(1)y_2+\mu(1))\,\rho_{2D}(y_1,y_2)\,dy_1dy_2 && (61)\\
Cov(4,5) &= \frac{1}{2}c_{pc}\sigma_{pc}^2 + \sigma_{pc}\frac{gIP}{2}\int \frac{y}{\sqrt{2}}F(\sigma(4)y+\mu(4))\,\rho_{SN}(y)\,dy && (62)\\
Cov(4,6) &= Cov(4,5) && (63)\\
Cov(5,6) &= \frac{1}{2}c_{pc}\sigma_{pc}^2 + \frac{g_{IP}^2}{2}Var\big(F(\sigma(4)Y+\mu(4))\big) \\
&\quad +\sigma_{pc}gIP\iint \frac{y_1}{\sqrt{2}}F(\sigma(4)y_2+\mu(4))\,\rho_{2D}(y_1,y_2)\,dy_1dy_2 && (64)
\end{aligned}
$$

Leaky Integrate-and-Fire Model of the OB–PC Circuit

We use a generic spiking neural network model of leaky integrate-and-fire neurons to test the results of the theory. There were $N_{OB} = 60$ total OB cells, of which we set 80% (48) to be excitatory and 20% (12) inhibitory. The equations for the OB cells are, indexed by $k \in \{1, 2, \ldots, N_{OB}\}$:

$$
\begin{aligned}
\tau_m\frac{dv_k}{dt} &= \mu_{OB} - v_k - g_{k,XI}(t)(v_k-\mathcal{E}_I) - g_{k,XE}(t)(v_k-\mathcal{E}_E) \\
&\quad -g_{k,XPC}(t-\tau_{\Delta,PC})(v_k-\mathcal{E}_E) + \sigma_{OB}\left(\sqrt{1-\tilde{c}_{OB}}\eta_k(t) + \sqrt{\tilde{c}_{OB}}\xi_o(t)\right) \\
v_k(t^*) &\geq \theta_k \Rightarrow v_k(t^*+\tau_{ref}) = 0 \\
g_{k,XE}(t) &= \frac{\gamma_{XE}}{p_{XE}\,(0.8N_{OB})}\sum_{k'\in\{\text{ presyn OB E-cells}\}} G_{k'}(t) \\
g_{k,XI}(t) &= \frac{\gamma_{XI}}{p_{XI}\,(0.2N_{OB})}\sum_{k'\in\{\text{presyn OB I-cells}\}} G_{k'}(t) \\
g_{k,XPC}(t) &= \frac{\gamma_{X,PC}}{p_{X,PC}\,(0.8N_{PC})}\sum_{j'\in\{\text{presyn PC E-cells}\}} G_{j'}(t) \\
\tau_{d,X}\frac{dG_k}{dt} &= -G_k + A_k \\
\tau_{r,X}\frac{dA_k}{dt} &= -A_k + \tau_{r,X}\alpha_X\sum_l \delta(t-t_{k,l}). && (65)
\end{aligned}
$$

The conductance values in the first equation $g_{k,XI}$, $g_{k,XE}$, and $g_{k,XPC}$ depend on the type of neuron v_k ($X \in \{E, I\}$). The last conductance, $g_{X,PC}(t-\tau_{\Delta,PC})(v_k-\mathcal{E}_E)$, models the excitatory presynaptic input (feedback) from the PC cells with a time delay of $\tau_{\Delta,PC}$. The conductance variables $g_{k,XY}(t)$ are dimensionless because this model was derived from scaling the original (raw) conductance variables by the leak conductance with the same dimension. The leak, inhibitory and excitatory reversal potentials are 0, $\mathcal{E}_I$, and $\mathcal{E}_E$, respectively with $\mathcal{E}_I < 0 < \mathcal{E}_E$ (the voltage is scaled to be dimensionless, see Table 4). $\xi_k(t)$ are uncorrelated white noise processes and $\xi_o(t)$ is the common noise term to all N_{OB} cells.

The second equation describes the refractory period at spike time t^*: when the neuron's voltage crosses threshold θ_j (see below for distribution of thresholds), the neuron goes into a refractory period for τ_{ref}, after which we set the neuron's voltage to 0.

The parameter γ_{XY} gives the relative weight of a connection from neuron type Y to neuron type X; the parameter p_{XY} is probability that any such connection exists ($X, Y \in \{E, I\}$). G_k is the synaptic variable associated with each cell, and dependent only on that cell's spike times; its dynamics are given by the final two equations in Eq 65 and depend on whether $k \in \{E, I\}$.

Finally, two of the parameters above can be equated with coupling parameters in the reduced model:

$$gEP = \gamma_{I,PC}; \quad gIO = \gamma_{EI} \tag{66}$$

which are dimensionless scale factors for the synaptic conductances.

Table 4. Fixed parameters for the LIF OB–PC model, see Eqs 65–67.

Same for both OB and PC										
Parameter	τ_m	τ_{ref}	$\mathcal{E}_I$	$\mathcal{E}_E$	$\tau_{d,I}$	$\tau_{r,I}$	$\tau_{d,E}$	$\tau_{r,E}$	α_I	α_E
	20 ms	2 ms	-2.5	6.5	10 ms	2 ms	5 ms	1 ms	2 Hz	1 Hz
Parameter	N	Spont. μ	Evoked μ	σ	$\tilde{c}$	γ_{EE}	γ_{IE}	γ_{II}	$\gamma_{E,PC/OB}$	$\tau_{\Delta,PC/OB}$
OB	60	0.6	0.9	0.05	0.5	2	4	6	1	10 ms
PC	100	0	0.4	0.1	0.8	2	4	6	1	5 ms

All 12 probabilities of connections are set to $p_{XY} = 0.30$ and were randomly chosen (Erdős-Rényi graphs). The synaptic time delay from OB to PC is $\tau_{\Delta,OB} = 10$ ms, and from PC to OB is $\tau_{\Delta,PC} = 5$ ms. The scaled voltages from mV is: (V+Vreset)/(Vth+Vreset), corresponding for example to Vreset=Vleak=-65 mV, Vth=-55 mV (on average), excitatory reversal potential of 0 mV and inhibitory reversal potential of -90 mV.

The PC cells had similar functional form but with different parameters (see Table 4 for parameter values). We modeled $N_{PC} = 100$ total PC cells, of which 80% were excitatory and 20% inhibitory. The equations, indexed by $j \in \{1, 2, \ldots, N_{PC}\}$ are:

$$\begin{aligned}
\tau_m \frac{dv_j}{dt} &= \mu_{PC} - v_j - g_{j,XI}(t)(v_j - \mathcal{E}_I) - g_{j,XE}(t)(v_j - \mathcal{E}_E) \\
&\quad -g_{j,XOB}(t - \tau_{\Delta,OB})(v_j - \mathcal{E}_E) + \sigma_{PC}\left(\sqrt{1-\tilde{c}_{PC}}\eta_j(t) + \sqrt{\tilde{c}_{PC}}\xi_p(t)\right) \\
v_j(t^*) &\geq \theta_j \Rightarrow v_j(t^* + \tau_{ref}) = 0 \\
g_{j,XE}(t) &= \frac{\gamma_{XE}}{p_{XE}\,(0.8N_{PC})} \sum_{j' \in \{\text{presyn PC E-cells}\}} G_{j'}(t) \\
g_{j,XI}(t) &= \frac{\gamma_{XI}}{p_{XI}\,(0.2N_{PC})} \sum_{j' \in \{\text{presyn PC I-cells}\}} G_{j'}(t) \\
g_{j,XOB}(t) &= \frac{\gamma_{X,OB}}{p_{X,OB}\,(0.8N_{OB})} \sum_{k' \in \{\text{presyn OB E-cells}\}} G_{k'}(t) \\
\tau_{d,X} \frac{dG_j}{dt} &= -G_j + A_j \\
\tau_{r,X} \frac{dA_j}{dt} &= -A_j + \tau_{r,X}\alpha_X \sum_l \delta(t - t_{j,l}).
\end{aligned} \tag{67}$$

Excitatory synaptic input from the OB cells along the lateral olfactory tract is modeled by: $g_{X,OB}(t - \tau_{\Delta,OB})(v_j - \mathcal{E}_E)$. The common noise term for the PC cells $\xi_p(t)$ is independent of the common noise term for the OB cells $\xi_o(t)$. Two of the parameters above can be equated with coupling parameters in the reduced model:

$$gEO = \gamma_{I,OB}; \quad gIP = \gamma_{EI} \tag{68}$$

The values of the parameters that were not stated in Table 4 were varied in the paper:

$$gIO, \qquad gEO, \qquad gIP, \qquad gEP.$$

To model two activity states, we allowed mean inputs to vary (see Table 4). In contrast to the reduced model, we increased both inputs to PC cells (from $\mu_{PC} = 0$ in the spontaneous state to $\mu_{PC} = 0.4$ in the evoked state) as well as to OB cells (from $\mu_{OB} = 0.6$ in the spontaneous state to $\mu_{OB} = 0.9$ in the evoked state).

Finally, we model heterogeneity by setting the threshold values θ_j in the following way. Both OB and PC cells had the following distributions for θ_j:

$$\theta_j \quad \sim \quad e^{\mathcal{N}} \tag{69}$$

where $\mathcal{N}$ is normal distribution with mean $-\sigma_\theta^2/2$ and standard deviation σ_θ, so that $\{\theta_j\}$ has a log-normal distribution with mean 1 and variance: $e^{\sigma_\theta^2} - 1$. We set $\sigma_\theta = 0.1$, which results in firing rates ranges seen in the experimental data. Since the number of cells are modest with regards to sampling ($N_{OB} = 60$, $N_{PC} = 100$), we evenly sampled the log-normal distribution from the 5^{th} to 95^{th} percentiles (inclusive).

We remark that the synaptic delays of $\tau_{\Delta,PC}$ and $\tau_{\Delta,OB}$ were set to modest values to capture the appreciable distances between OB and PC. This is a reasonable choice based on evidence that stimulation in PC illicit a response in OB 5-10 ms later [51].

In all Monte Carlo simulations of the coupled LIF network, we used a time step of 0.1 ms, with 2 s of biology time for each of the 100,000 realizations (i.e., over 55.5 hours of biology time), enough simulated statistics to effectively have convergence.

Supporting Information

S1 Text. Experimental Data Statistics by Odor. This file shows the trial-averaged spiking statistics of the experimental data dissected by a specific odor. Contains captions for Fig. S1-S8.

S2 Text. Supplementary Figures for Modeling and Analysis. This file contains supplemental figures from modeling and analysis. Contains captions for Fig. S9-S16.

S1 Figure. Experimental statistics by odor and activity state: Fano Factor.

S2 Figure. Experimental statistics by odor and activity state: spike count variance.

S3 Figure. Experimental statistics by odor and region: Fano Factor.

S4 Figure. Experimental statistics by odor and region: spike count variance.

S5 Figure. Experimental statistics by odor and activity state: spike count correlation.

S6 Figure. Experimental statistics by odor and activity state: spike count covariance.

S7 Figure. Experimental statistics by odor and region: spike count correlation.

S8 Figure. Experimental statistics by odor and region: spike count covariance.

S9 Figure. Cross-region correlations are smaller than within-region correlations.

S10 Figure. Fast analytic approximation accurately captures statistics of a multi-population firing rate model.

S11 Figure. Experimental observations constrain conductance parameters in analytic model.

S12 Figure. Analytic approximation results are robust to choice of transfer function.

S13 Figure. Mean input to PC must increase in the evoked state.

S14 Figure. Violating derived relationship $gIO < gIP$ results in statistics that are inconsistent with experimental observations.

S15 Figure. Violating derived relationship $gEP > gEO$ results in statistics that are inconsistent with experimental observations.

S16 Figure. Violating derived relationship $gEP, gIP \gg gEO, gIO$ results in statistics that are inconsistent with experimental observations.

Acknowledgments

Author Contributions

Conceived and designed research: AKB CL. Derived expressions in theoretical methods: CL. Analyzed the data: AKB SHG WLS CL. Conceived and designed electrophysiological experiments: SHG WLS. Wrote the paper: AKB SHG WLS CL.

References

1. A. Abouzeid and B. Ermentrout. Type-ii phase resetting curve is optimal for stochastic synchrony. *Physical Review E*, 80(1):011911, 2009.
2. Misha B Ahrens, Michael B Orger, Drew N Robson, Jennifer M Li, and Philipp J Keller. Whole-brain functional imaging at cellular resolution using light-sheet microscopy. *Nature methods*, 10(5):413–420, 2013.
3. W. Bair, E. Zohary, and W.T. Newsome. Correlated firing in macaque visual area mt: time scales and relationship to behavior. *The Journal of Neuroscience*, 21(5):1676–1697, 2001.
4. A. K. Barreiro, E. Shea-Brown, and E.L. Thilo. Time scales of spike-train correlation for neural oscillators with common drive. *Physical Review E*, 81:011916, 2010.
5. A.K. Barreiro, E.L. Thilo, and E. Shea-Brown. A-current and type i/type ii transition determine collective spiking from common input. *Journal of Neurophysiology*, 108(6):1631, 2012.
6. Alison M Boyd, James F Sturgill, Cindy Poo, and Jeffry S Isaacson. Cortical feedback control of olfactory bulb circuits. *Neuron*, 76(6):1161–1174, 2012.
7. Paul C Bressloff. Stochastic neural field theory and the system-size expansion. *SIAM Journal on Applied Mathematics*, 70(5):1488–1521, 2009.
8. N. Brunel. Dynamics of sparsely connected networks of excitatory and inhibitory spiking neurons. *Journal of Computational Neuroscience*, 8:183–208, 2000.
9. N. Brunel and V. Hakim. Fast global oscillations in networks of integrate-and-fire neurons with low firing rates. *Neural Computation*, 11:1621–1671, 1999.
10. M.A. Buice, J.D. Cowan, and C.C. Chow. Systematic fluctuation expansion for neural network activity equations. *Neural Computation*, 22:377–426, 2010.

11. Michael A Buice and Jack D Cowan. Field-theoretic approach to fluctuation effects in neural networks. *Physical Review E*, 75(5):051919, 2007.

12. Shawn D Burton and Nathaniel N Urban. Rapid feedforward inhibition and asynchronous excitation regulate granule cell activity in the mammalian main olfactory bulb. *The Journal of Neuroscience*, 35(42):14103–14122, 2015.

13. Jessica A Cardin, Larry A Palmer, and Diego Contreras. Cellular mechanisms underlying stimulus-dependent gain modulation in primary visual cortex neurons in vivo. *Neuron*, 59(1):150–160, 2008.

14. M.M. Churchland, B.M. Yu, et al. Stimulus onset quenches neural variability: a widespread cortical phenomenon. *Nature Neuroscience*, 13:369–378, 2010.

15. M.R. Cohen and A. Kohn. Measuring and interpreting neuronal correlations. *Nature Neuroscience*, 14:811–819, 2011.

16. M.R. Cohen and J.HR. Maunsell. Attention improves performance primarily by reducing interneuronal correlations. *Nature Neuroscience*, 12:1594–1600, 2009.

17. Kevin M Cury and Naoshige Uchida. Robust odor coding via inhalation-coupled transient activity in the mammalian olfactory bulb. *Neuron*, 68(3):570–585, 2010.

18. P. Dayan and L.F. Abbott. *Theoretical neuroscience: Computational and mathematical modeling of neural systems*. Taylor & Francis, 2001.

19. B. Doiron, A. Litwin-Kumar, R. Rosenbaum, G. Ocker, and K. Josić. The mechanics of state-dependent neural correlations. *Nature Neuroscience*, 19(3):383–393, 2016.

20. A. Ecker, P. Berens, A. Tolias, and M. Bethge. The effect of noise correlations in populations of diversely tuned neurons. *The Journal of Neuroscience*, 31(40):14272–14283, 2011.

21. O. Faugeras, J. Touboul, and B. Cessac. A constructive mean-field analysis of multi-population neural networks with random synaptic weights and stochastic inputs. *Frontiers in Computational Neuroscience*, 3, 2009.

22. J-M Fellous, Michael Rudolph, Alain Destexhe, and Terrence J Sejnowski. Synaptic background noise controls the input/output characteristics of single cells in an in vitro model of in vivo activity. *Neuroscience*, 122(3):811–829, 2003.

23. Rainer W Friedrich and Gilles Laurent. Dynamic optimization of odor representations by slow temporal patterning of mitral cell activity. *Science*, 291(5505):889–894, 2001.

24. C.W. Gardiner. *Handbook of stochastic methods*. Springer-Verlag, 1985.

25. Shree Hari Gautam, Thanh T Hoang, Kylie McClanahan, Stephen K Grady, and Woodrow L Shew. Maximizing sensory dynamic range by tuning the cortical state to criticality. *PLoS Computational Biology*, 11(12):e1004576, 2015.

26. Shree Hari Gautam and Justus V Verhagen. Retronasal odor representations in the dorsal olfactory bulb of rats. *The Journal of Neuroscience*, 32(23):7949–7959, 2012.

27. Agnieszka Grabska-Barwińska, Simon Barthelmé, Jeff Beck, Zachary F Mainen, Alexandre Pouget, and Peter E Latham. A probabilistic approach to demixing odors. *Nature Neuroscience*, 20:98–106, 2017.

28. Olivier Gschwend, Jonathan Beroud, and Alan Carleton. Encoding odorant identity by spiking packets of rate-invariant neurons in awake mice. *PloS one*, 7(1):e30155, 2012.

29. Sungho Hong, Stéphanie Ratté, Steven A Prescott, and Erik De Schutter. Single neuron firing properties impact correlation-based population coding. *The Journal of Neuroscience*, 32(4):1413–1428, 2012.

30. Stojan Jovanović and Stefan Rotter. Interplay between graph topology and correlations of third order in spiking neuronal networks. *PLOS Computational Biology*, 12(6):e1004963, 2016.

31. J.Touboul and B. Ermentrout. Finite-size and correlation-induced effects in mean-field dynamics. *Journal of Computational Neuroscience*, 31:453–484, 2011.

32. Eric R Kandel, Henry Markram, Paul M Matthews, Rafael Yuste, and Christof Koch. Neuroscience thinks big (and collaboratively). *Nature Reviews Neuroscience*, 14(9):659–664, 2013.

33. S.M. Kay. *Fundamentals of Statistical Signal Processing, Volume 1: Estimation Theory*. Prentice Hall PTR, 1993.

34. Adam Kohn, Ruben Coen-Cagli, Ingmar Kanitscheider, and Alexandre Pouget. Correlations and neuronal population information. *Annual review of neuroscience*, 39(0), 2016.

35. A. Large, N. Vogler, S. Mielo, and A.M.M. Oswald. Balanced feedforward inhibition and dominant recurrent inhibition in olfactory cortex. *Proceedings of the National Academy of Sciences*, 113(8):2276–2281, 2016.

36. William C Lemon, Stefan R Pulver, Burkhard Höckendorf, Katie McDole, Kristin Branson, Jeremy Freeman, and Philipp J Keller. Whole-central nervous system functional imaging in larval drosophila. *Nature communications*, 6, 2015.

37. A. Litwin-Kumar, M. Chacron, and B. Doiron. The spatial structure of stimuli shapes the timescale of correlations in population spiking activity. *PLoS Computational Biology*, 8(9):e1002667, 2012.

38. A. Litwin-Kumar and B. Doiron. Slow dynamics and high variability in balanced cortical networks with clustered connections. *Nature Neuroscience*, 15(11):1498–1505, 2012.

39. A. Litwin-Kumar, AM.M. Oswald, N.N. Urban, and B. Doiron. Balanced synaptic input shapes the correlation between neural spike trains. *PLoS Computational Biology*, 7:e1002305, 2011.

40. C. Ly and B. Ermentrout. Synchronization dynamics of two coupled neural oscillators receiving shared and unshared noisy stimuli. *Journal of Computational Neuroscience*, 26:425–443, 2009.

41. C. Ly, J.W. Middleton, and B. Doiron. Cellular and circuit mechanisms maintain low spike co-variability and enhance population coding in somatosensory cortex. *Frontiers in Computational Neuroscience*, 6:1–26, 2012.

42. C. Ly and D. Tranchina. Critical Analysis of Dimension Reduction by a Moment Closure Method in a Population Density Approach to Neural Network Modeling. *Neural Computation*, 19:2032–2092, 2007.

43. S. Marella and B. Ermentrout. Class-ii neurons display a higher degree of stochastic synchronization than class-i neurons. *Physical Review E*, 77:041918, 2008.

44. Foivos Markopoulos, Dan Rokni, David H Gire, and Venkatesh N Murthy. Functional properties of cortical feedback projections to the olfactory bulb. *Neuron*, 76(6):1175–1188, 2012.

45. Alexander Mathis, Dan Rokni, Vikrant Kapoor, Matthias Bethge, and Venkatesh N Murthy. Reading out olfactory receptors: feedforward circuits detect odors in mixtures without demixing. *Neuron*, 91:1110–1123, 2016.

46. J.W. Middleton, C. Omar, and B. Doiron D.J. Simons. Neural correlation is stimulus modulated by feedforward inhibitory circuitry. *The Journal of Neuroscience*, 32:506–518, 2012.

47. Jude F Mitchell, Kristy A Sundberg, and John H Reynolds. Spatial attention decorrelates intrinsic activity fluctuations in macaque area v4. *Neuron*, 63(6):879–888, 2009.

48. K. Miura, Z. Mainen, and N. Uchida. Odor representations in olfactory cortex: distributed rate coding and decorrelated population activity. *Neuron*, 74:1087–1098, 2012.

49. Rubén Moreno-Bote, Jeffrey Beck, Ingmar Kanitscheider, Xaq Pitkow, Peter Latham, and Alexandre Pouget. Information-limiting correlations. *Nature neuroscience*, 17(10):1410–1417, 2014.

50. Masayoshi Murakami, Hideki Kashiwadani, Yutaka Kirino, and Kensaku Mori. State-dependent sensory gating in olfactory cortex. *Neuron*, 46(2):285–296, 2005.

51. Kevin R Neville and Lewis B Haberly. Beta and gamma oscillations in the olfactory system of the urethane-anesthetized rat. *Journal of Neurophysiology*, 90(6):3921–3930, 2003.

52. W. Nicola, C. Ly, and S. A. Campbell. One-dimensional population density approaches to recurrently coupled networks of neurons with noise. *SIAM Journal on Applied Mathematics*, 75:2333–2360, 2015.

53. Gabriel Koch Ocker and Brent Doiron. Kv7 channels regulate pairwise spiking covariability in health and disease. *Journal of neurophysiology*, 112(2):340–352, 2014.

54. Ifije E Ohiorhenuan, Ferenc Mechler, Keith P Purpura, Anita M Schmid, Qin Hu, and Jonathan D Victor. Sparse coding and high-order correlations in fine-scale cortical networks. *Nature*, 466(7306):617–621, 2010.

55. S. Ostojic, N. Brunel, and V. Hakim. How connectivity, background activity, and synaptic properties shape the cross-correlation between spike trains. *The Journal of Neuroscience*, 29:10234–10253, 2009.

56. C. Poo and J. Isaacson. Odor representations in olfactory cortex:?sparse? coding, global inhibition, and oscillations. *Neuron*, 62:850–861, 2009.

57. Steven A Prescott and Yves De Koninck. Gain control of firing rate by shunting inhibition: roles of synaptic noise and dendritic saturation. *Proceedings of the National Academy of Sciences*, 100(4):2076–2081, 2003.

58. Robert Prevedel, Young-Gyu Yoon, Maximilian Hoffmann, Nikita Pak, Gordon Wetzstein, Saul Kato, Tina Schrödel, Ramesh Raskar, Manuel Zimmer, Edward S Boyden, et al. Simultaneous whole-animal 3d imaging of neuronal activity using light-field microscopy. *Nature methods*, 11(7):727–730, 2014.

59. A. Renart, J. de la Rocha, P. Bartho, L. Hollender, N. Parga, A. Reyes, and K.D. Harris. The asynchronous state in cortical circuits. *Science*, 327:587–590, 2010.

60. R. Rosenbaum, J. Trousdale, and K. Josić. Pooling and correlated neural activity. *Frontiers in Computational Neuroscience*, 4, 2010.

61. Robert Rosenbaum, Jonathan E Rubin, and Brent Doiron. Short-term synaptic depression and stochastic vesicle dynamics reduce and shape neuronal correlations. *Journal of neurophysiology*, 109(2):475–484, 2013.

62. Robert Rosenbaum, Matthew A Smith, Adam Kohn, Jonathan E Rubin, and Brent Doiron. The spatial structure of correlated neuronal variability. *Nature Neuroscience*, 20(1):107–114, 2017.

63. C Rossant, SN Kadir, DF Goodman, J Schulman, ML Hunter, AB Saleem, A Grosmark, M Belluscio, GH Denfield, AS Ecker, AS Tolias, S Solomon, G Buzsáki, M Carandini, and KD Harris. Spike sorting for large, dense electrode arrays. *Nature neuroscience*, 19(4):634–641, 2016.

64. Douglas A Ruff and Marlene R Cohen. Attention can either increase or decrease spike count correlations in visual cortex. *Nature neuroscience*, 17(11):1591–1597, 2014.

65. Elad Schneidman, Michael J Berry, Ronen Segev, and William Bialek. Weak pairwise correlations imply strongly correlated network states in a neural population. *Nature*, 440(7087):1007–1012, 2006.

66. T. Tetzlaff, M. Helias, G.T. Einevoll, and M. Diesmann. Decorrelation of neural-network activity by inhibitory feedback. *PLoS Computational Biology*, 8:e1002596, 2012.

67. Taro Toyoizumi, Kamiar Rahnama Rad, and Liam Paninski. Mean-field approximations for coupled populations of generalized linear model spiking neurons with markov refractoriness. *Neural computation*, 21(5):1203–1243, 2009.

68. James Trousdale, Yu Hu, Eric Shea-Brown, and Krešimir Josić. Impact of network structure and cellular response on spike time correlations. *PLoS Comput Biol*, 8(3):e1002408, 2012.

69. James Trousdale, Yu Hu, Eric Shea-Brown, and Krešimir Josić. A generative spike train model with time-structured higher order correlations. *Frontiers in computational neuroscience*, 7, 2013.

70. Wilson Truccolo, Uri T Eden, Matthew R Fellows, John P Donoghue, and Emery N Brown. A point process framework for relating neural spiking activity to spiking history, neural ensemble, and extrinsic covariate effects. *Journal of neurophysiology*, 93(2):1074–1089, 2005.

71. H. R. Wilson and J. D. Cowan. Excitatory and inhibitory interactions in localized populations of model neurons. *Biophysical Journal*, 12:1–24, 1972.

72. E Zohary, MN Shadlen, and WT Newsome. Correlated neuronal discharge rate and its implications for psychophysical performance. *Nature*, 370(6485):140–143, 1994.

Experimental Data Statistics by Odor

Andrea K. Barreiro[#] ; Shree Hari Gautam[‡] ; Woodrow L. Shew[‡] ; Cheng Ly[†]

 # Department of Mathematics, Southern Methodist University, Dallas, TX 75275 U.S.A.
‡Department of Physics, University of Arkansas, Fayetteville, AR 72701 U.S.A.
†Department of Statistical Sciences and Operations Research, Virginia Commonwealth University, Richmond, VA 23284 U.S.A.
∗ E-mail: abarreiro@smu.edu ; shgautam@uark.edu; woodrowshew@gmail.com ; CLy@vcu.edu

Table S1. Average population firing rate (Hz) by odor and activity state.

Mean across population	All Odors	Odor 1	Odor 2	Odor 3	Odor 4
ν_{OB}^{Sp}	1.97	1.44	1.8	2.62	2.24
ν_{OB}^{Ev}	4.66	4.91	3.28	5.41	5.34
ν_{PC}^{Sp}	0.75	0.56	0.91	0.74	0.79
ν_{PC}^{Ev}	1.45	1.6	1.26	1.7	1.23

Table S2. Standard deviation of firing rate across the population (Hz) by odor and activity state.

Std. Dev. across population	All Odors	Odor 1	Odor 2	Odor 3	Odor 4
ν_{OB}^{Sp}	3.28	2.34	3.07	4.32	3.58
ν_{OB}^{Ev}	7.14	7.55	5.55	8	8.04
ν_{PC}^{Sp}	0.93	0.83	1.08	0.96	0.95
ν_{PC}^{Ev}	1.58	2.09	1.45	1.93	1.18

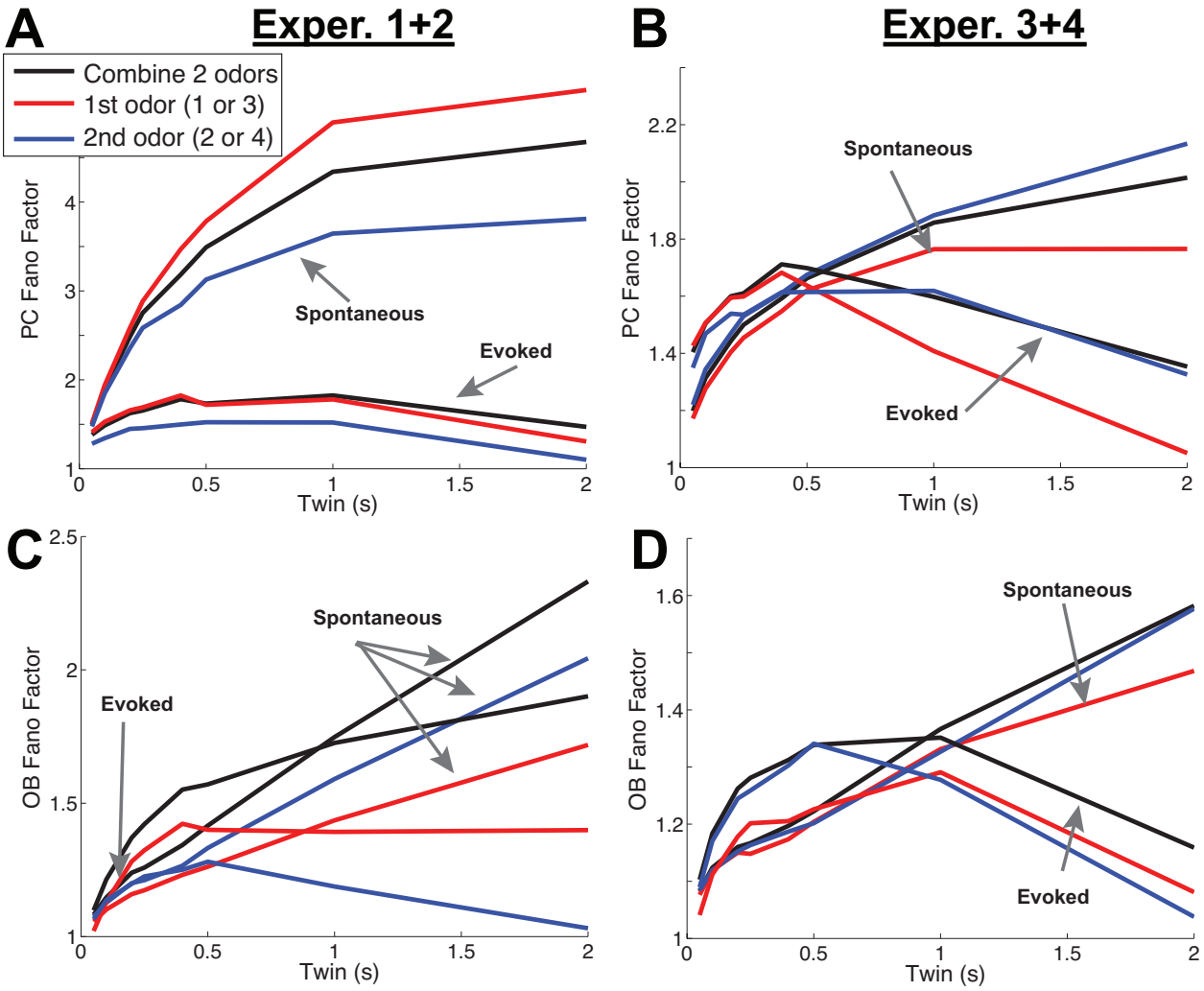

Fig S1. Experimental statistics by odor and activity state: Fano Factor. Comparing the **mean** Fano Factor across all simultaneously cells with: i) pairs from the 2 stimuli (black), ii) from the first odor (red), iii) from the second odor (blue). A and B are the PC cells, C and D are the OB cells. The left column A), C) is from `data040515_exp1+2.mat`, and the right column B), D) is from `data040515_exp3+4.mat` The spontaneous and evoked states in groups of 3 curves are denoted by the gray arrows.

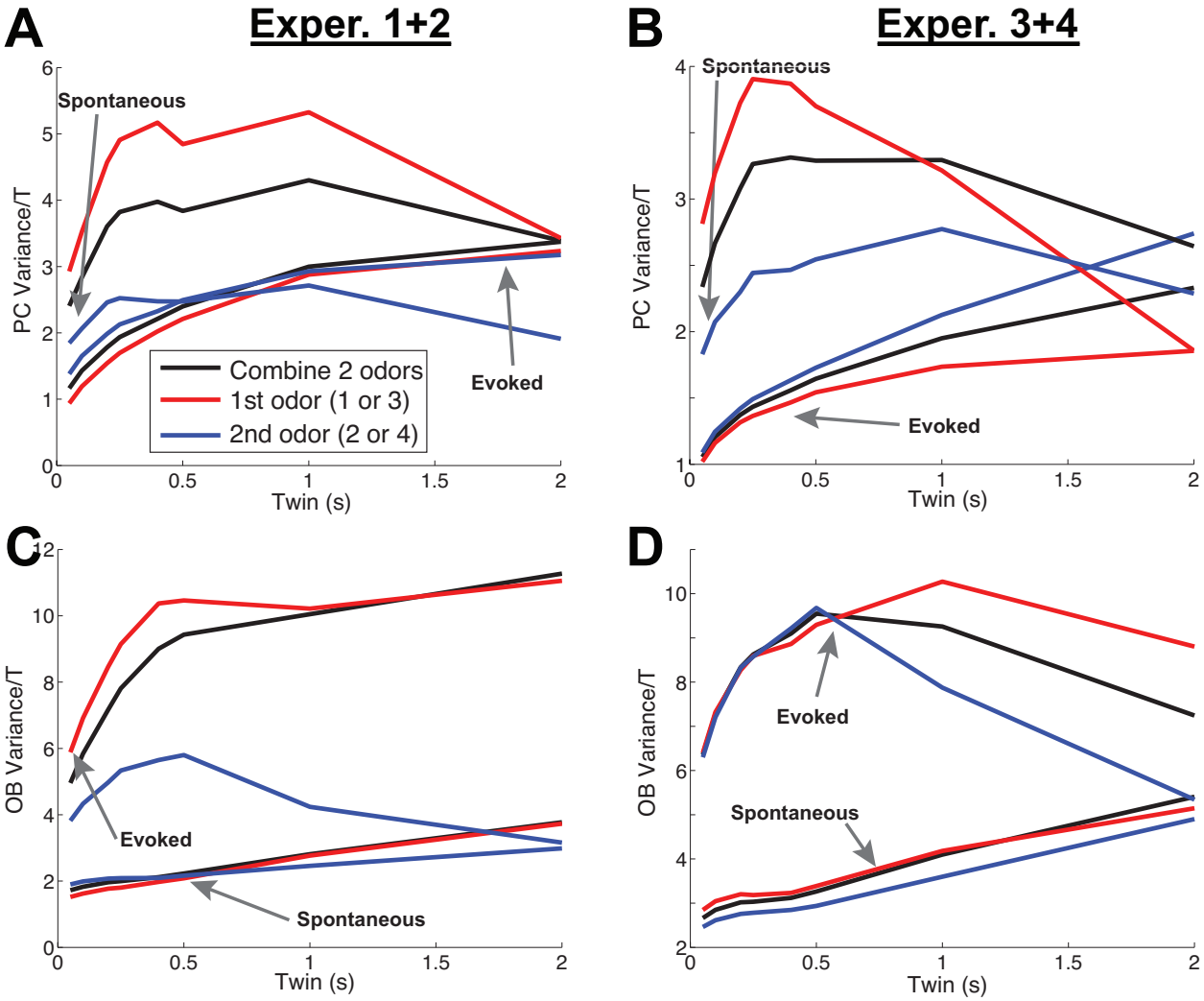

Fig S2. Experimental statistics by odor and activity state: spike count variance. Similar to Fig. S1 but comparing the **mean** variance divided by time window across all simultaneously cells with: i) pairs from the 2 stimuli (black), ii) from the first odor (red), iii) from the second odor (blue). A and B are the PC cells, C and D are the OB cells. The left column A), C) is from `data040515_exp1+2.mat`, and the right column B), D) is from `data040515_exp3+4.mat` The spontaneous and evoked states in groups of 3 curves are denoted by the gray arrows.

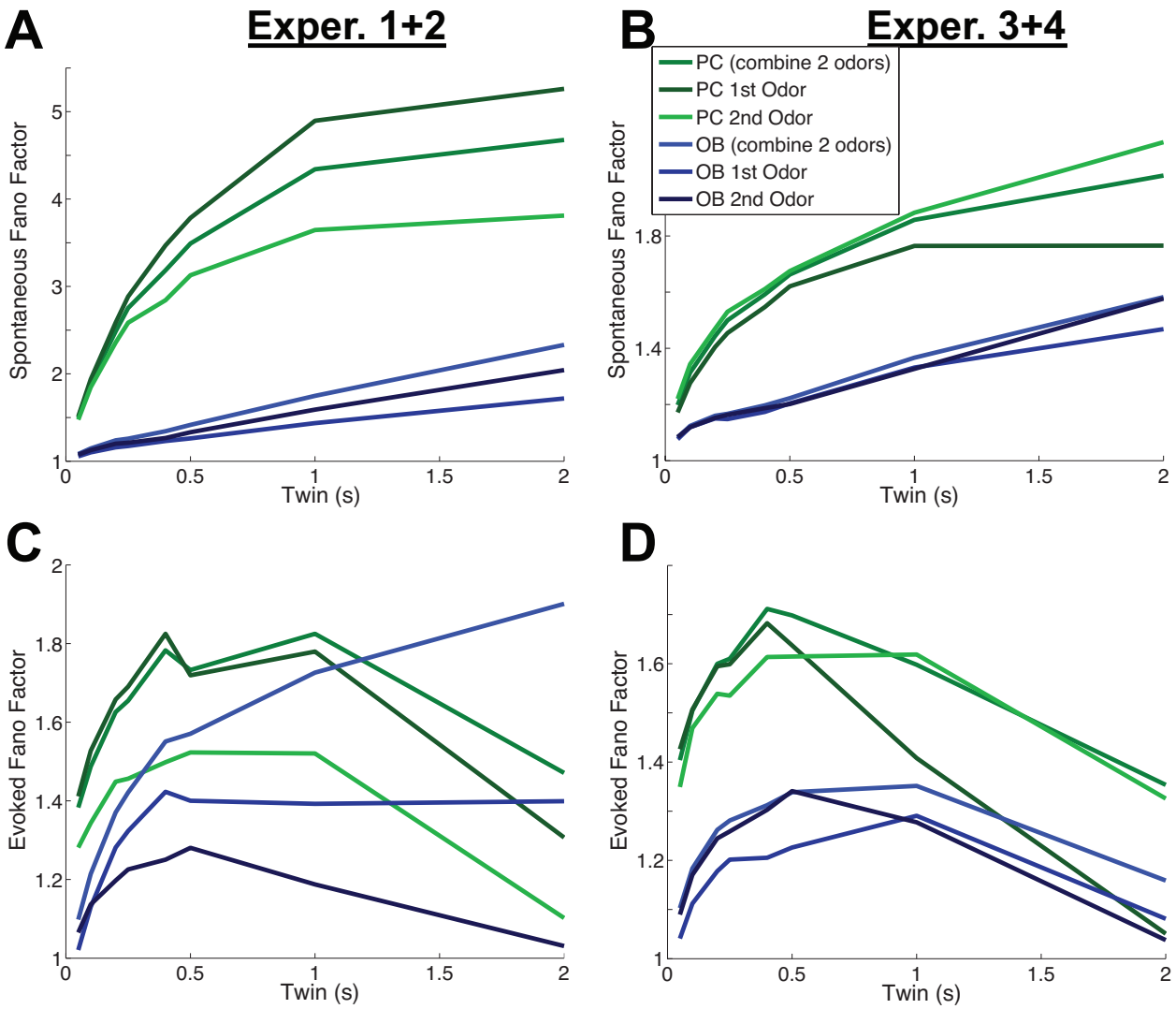

Fig S3. Experimental statistics by odor and region: Fano Factor. Comparing the **mean** Fano Factor between recorded PC (3 green curve) and OB (3 blue curves) cells, with: i) pairs from the 2 stimuli , ii) from the first odor, iii) from the second odor (see figure legend for color convention). A and B is for the spontaneous state, C and D is for the evoked state. The left column A), C) is from `data040515_exp1+2.mat`, and the right column B), D) is from `data040515_exp3+4.mat`.

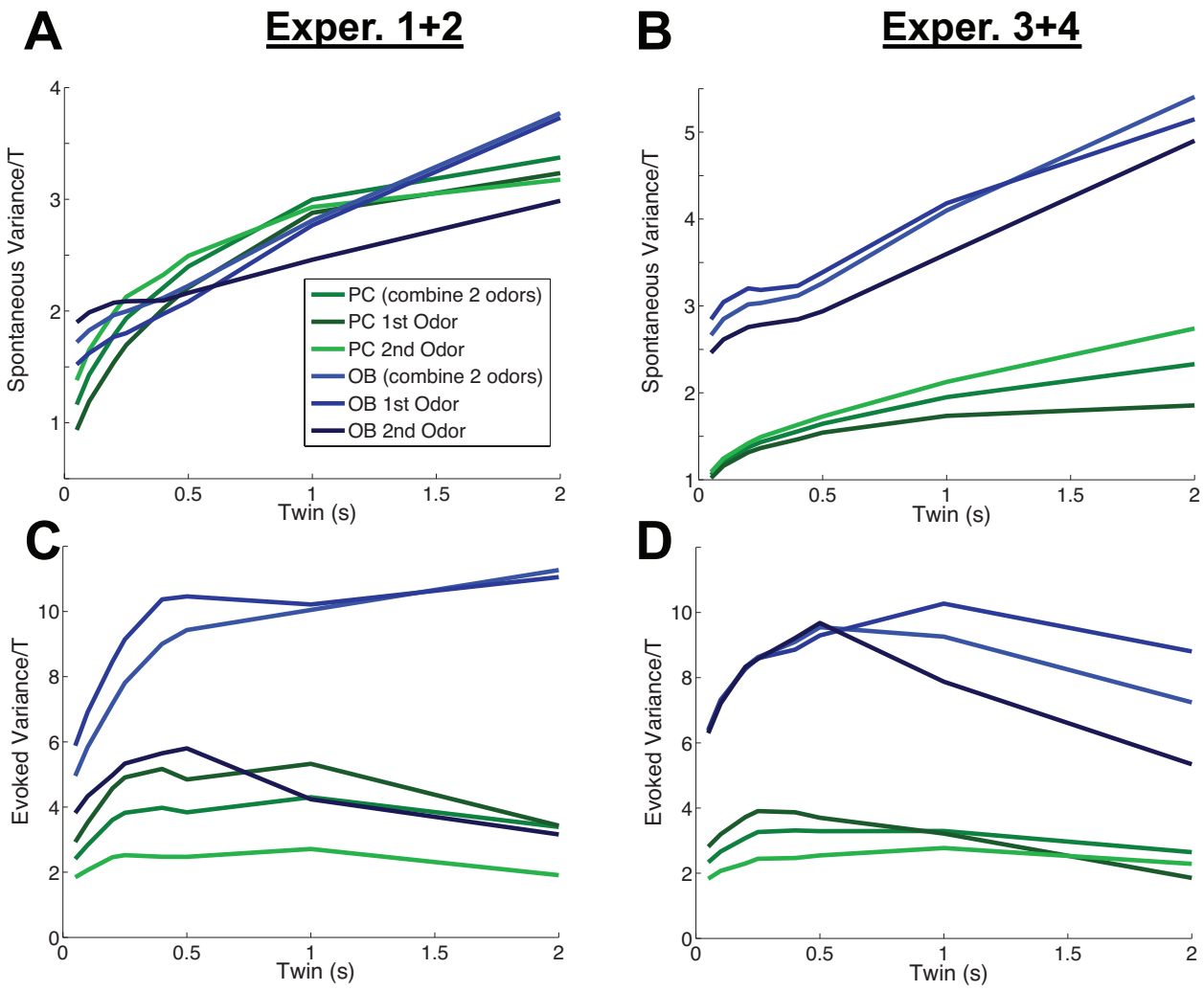

Fig S4. Experimental statistics by odor and region: spike count variance. Comparing the **mean** variance divided by time window between recorded PC (3 green curve) and OB (3 blue curves) cells, with: i) pairs from the 2 stimuli , ii) from the first odor, iii) from the second odor (see figure legend for color convention). A and B is for the spontaneous state, C and D is for the evoked state. The left column A), C) is from `data040515_exp1+2.mat`, and the right column B), D) is from `data040515_exp3+4.mat`.

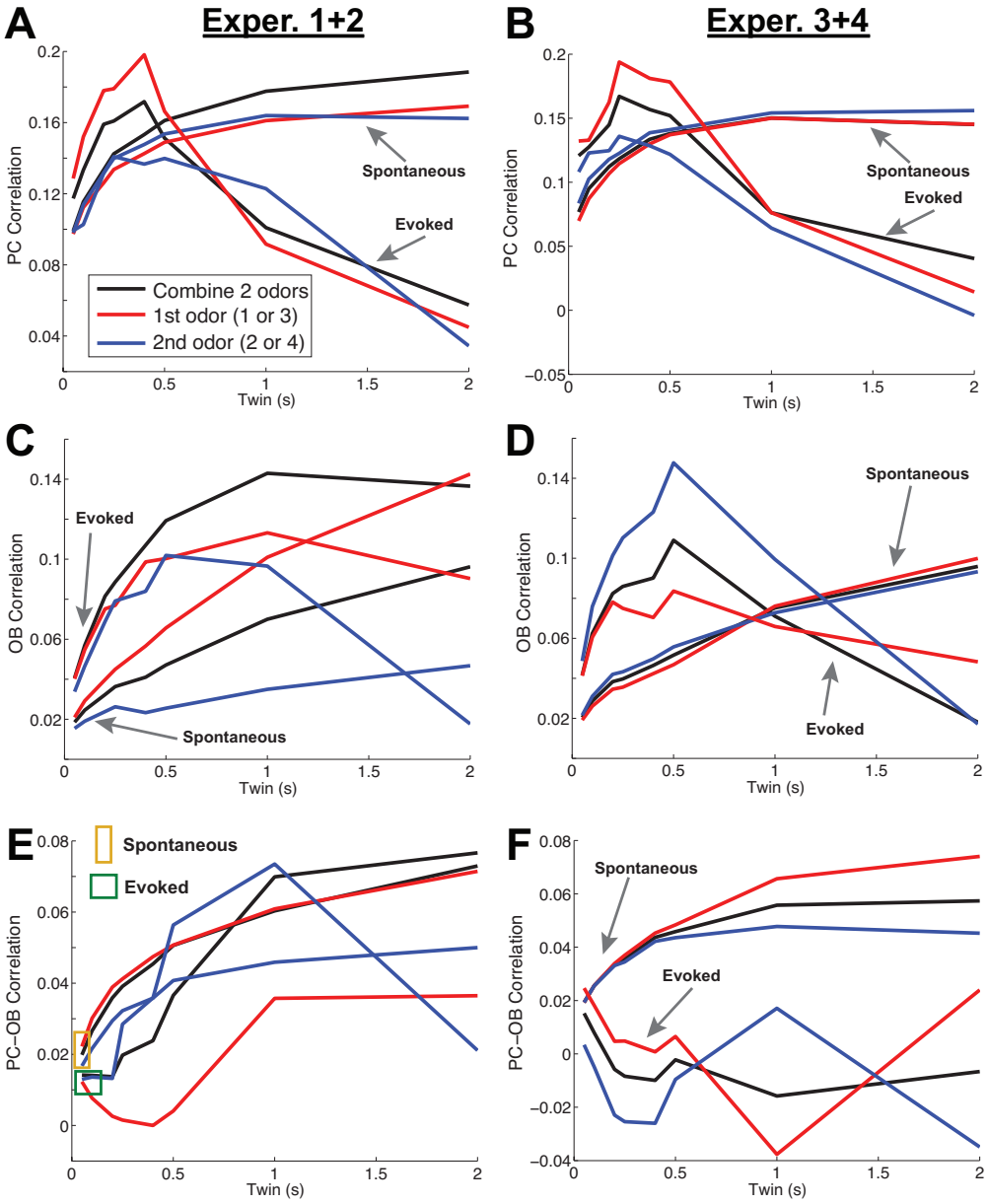

Fig S5. Experimental statistics by odor and activity state: spike count correlation. Comparing the **mean** spike count correlation across all simultaneously recorded pairs with: i) pairs from the 2 stimuli (black), ii) from the first odor (red), iii) from the second odor (blue). The left column A), C), E) is from `data040515_exp1+2.mat`, and the right column B), D), F) is from `data040515_exp3+4.mat` The spontaneous and evoked states in groups of 3 curves are denoted by the gray arrows.

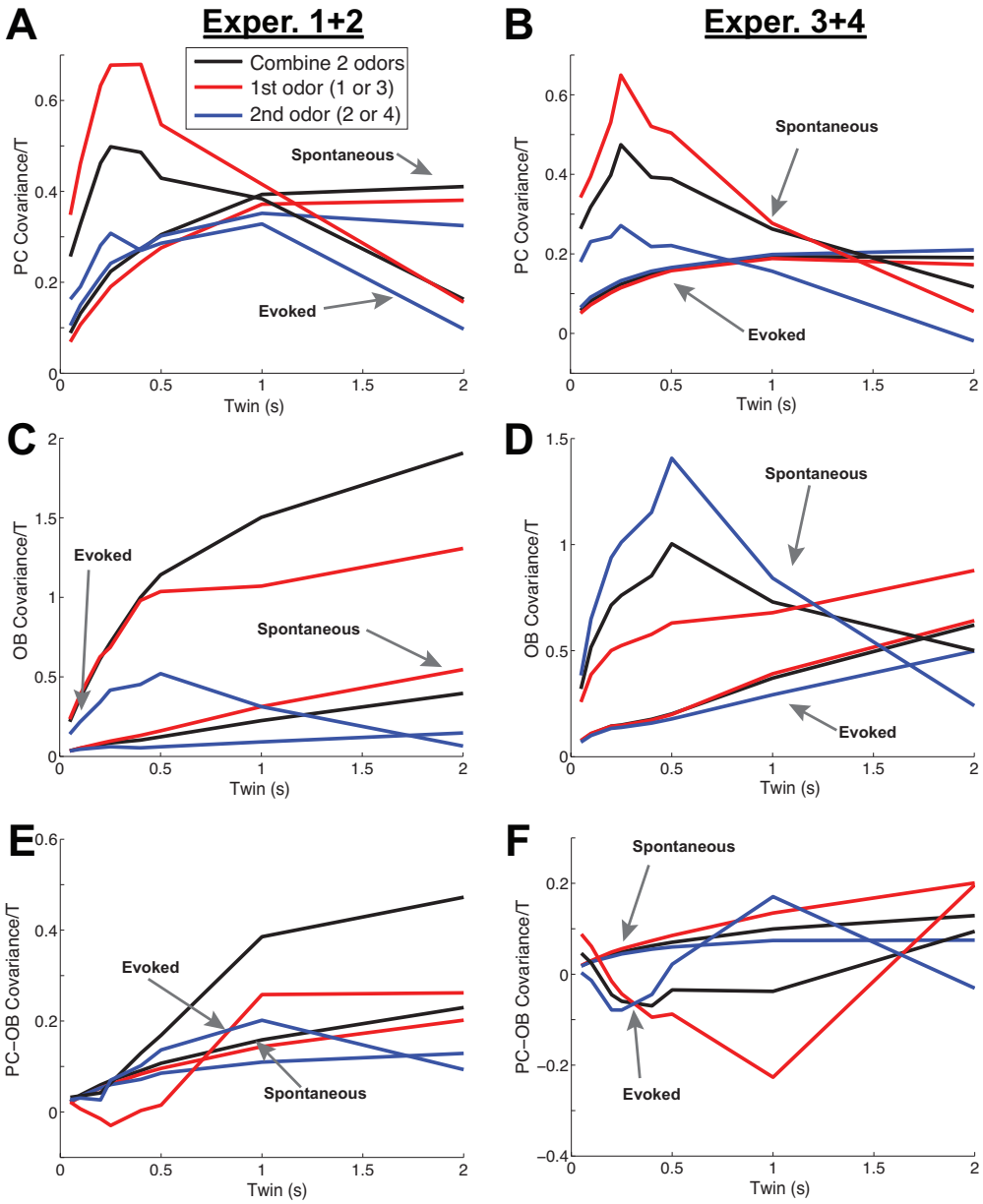

Fig S6. Experimental statistics by odor and activity state: spike count covariance. Similar to Fig. S5 but comparing the **mean** spike count covariance divided by time window across all simultaneously recorded pairs with: i) pairs from the 2 stimuli (black), ii) from the first odor (red), iii) from the second odor (blue). The left column A), C), E) is from `data040515_exp1+2.mat`, and the right column B), D), F) is from `data040515_exp3+4.mat` The spontaneous and evoked states in groups of 3 curves are denoted by the gray arrows.

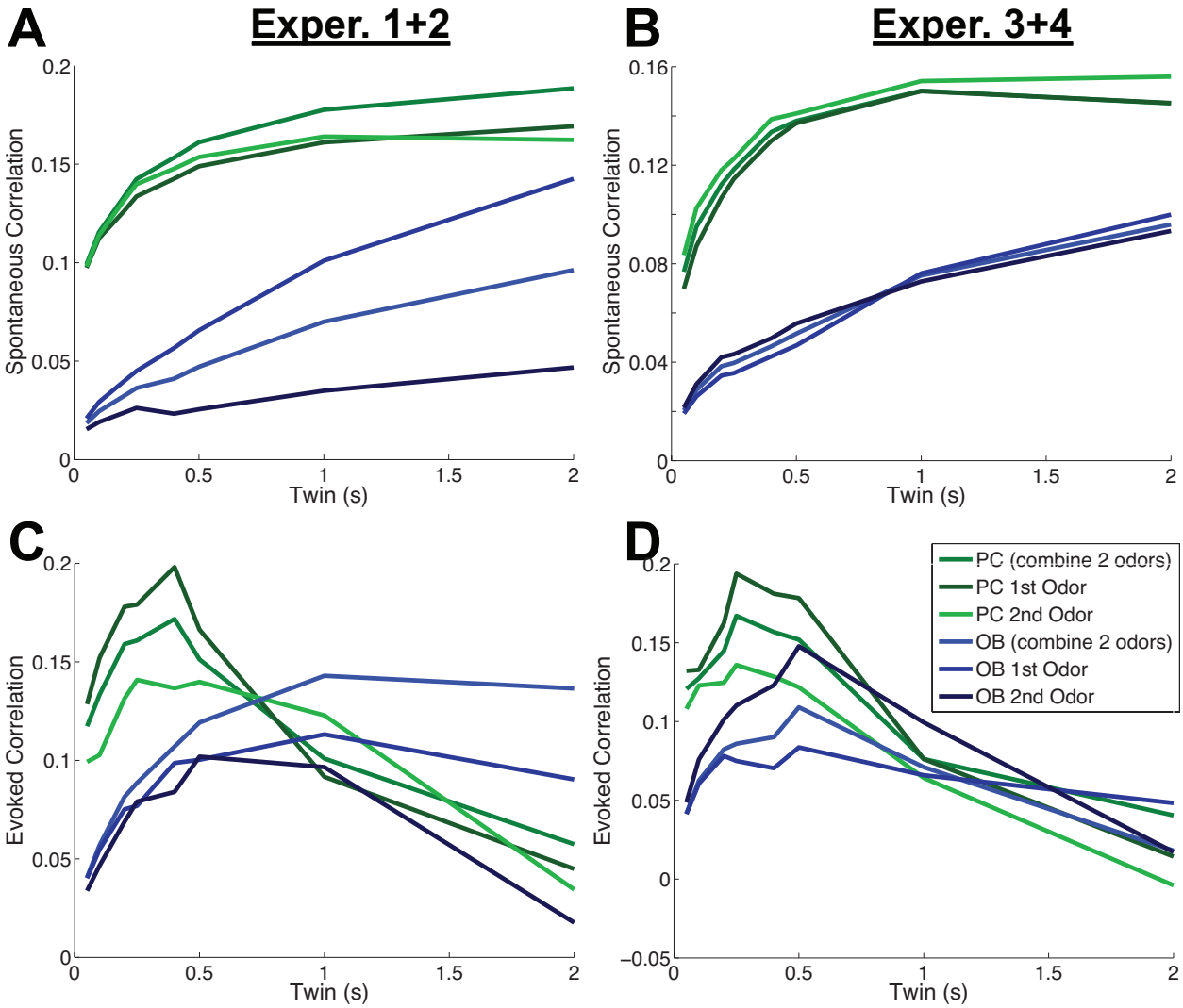

Fig S7. Experimental statistics by odor and region: spike count correlation. Comparing the **mean** spike count correlation between all pairs of PC (3 green curve) and OB (3 blue curves) cells, with: i) pairs from the 2 stimuli , ii) from the first odor, iii) from the second odor (see figure legend for color convention). The left column A), C), E) is from `data040515_exp1+2.mat`, and the right column B), D), F) is from `data040515_exp3+4.mat`.

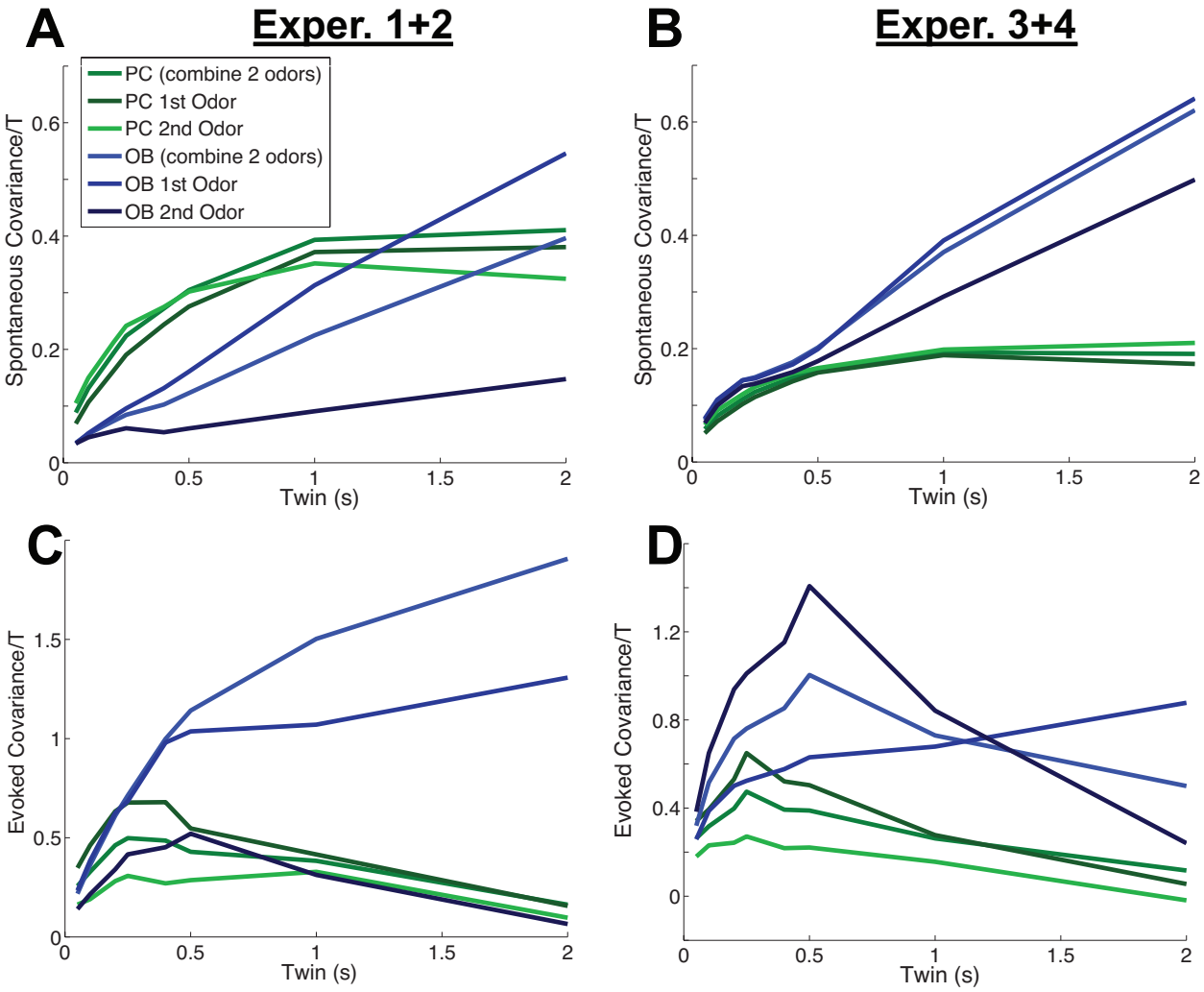

Fig S8. Experimental statistics by odor and region: spike count covariance. Comparing the **mean** spike count covariance divided by time window between all pairs of PC (3 green curve) and OB (3 blue curves) cells, with: i) pairs from the 2 stimuli , ii) from the first odor, iii) from the second odor (see figure legend for color convention). The left column A), C), E) is from `data040515_exp1+2.mat`, and the right column B), D), F) is from `data040515_exp3+4.mat`.

Supplementary Figures for Modeling and Analysis

Andrea K. Barreiro[#] ; Shree Hari Gautam[‡] ; Woodrow L. Shew[‡] ; Cheng Ly[†]

 # Department of Mathematics, Southern Methodist University, Dallas, TX 75275 U.S.A.
‡Department of Physics, University of Arkansas, Fayetteville, AR 72701 U.S.A.
†Department of Statistical Sciences and Operations Research, Virginia Commonwealth University, Richmond, VA 23284 U.S.A.
∗ E-mail: abarreiro@smu.edu ; shgautam@uark.edu; woodrowshew@gmail.com ; CLy@vcu.edu

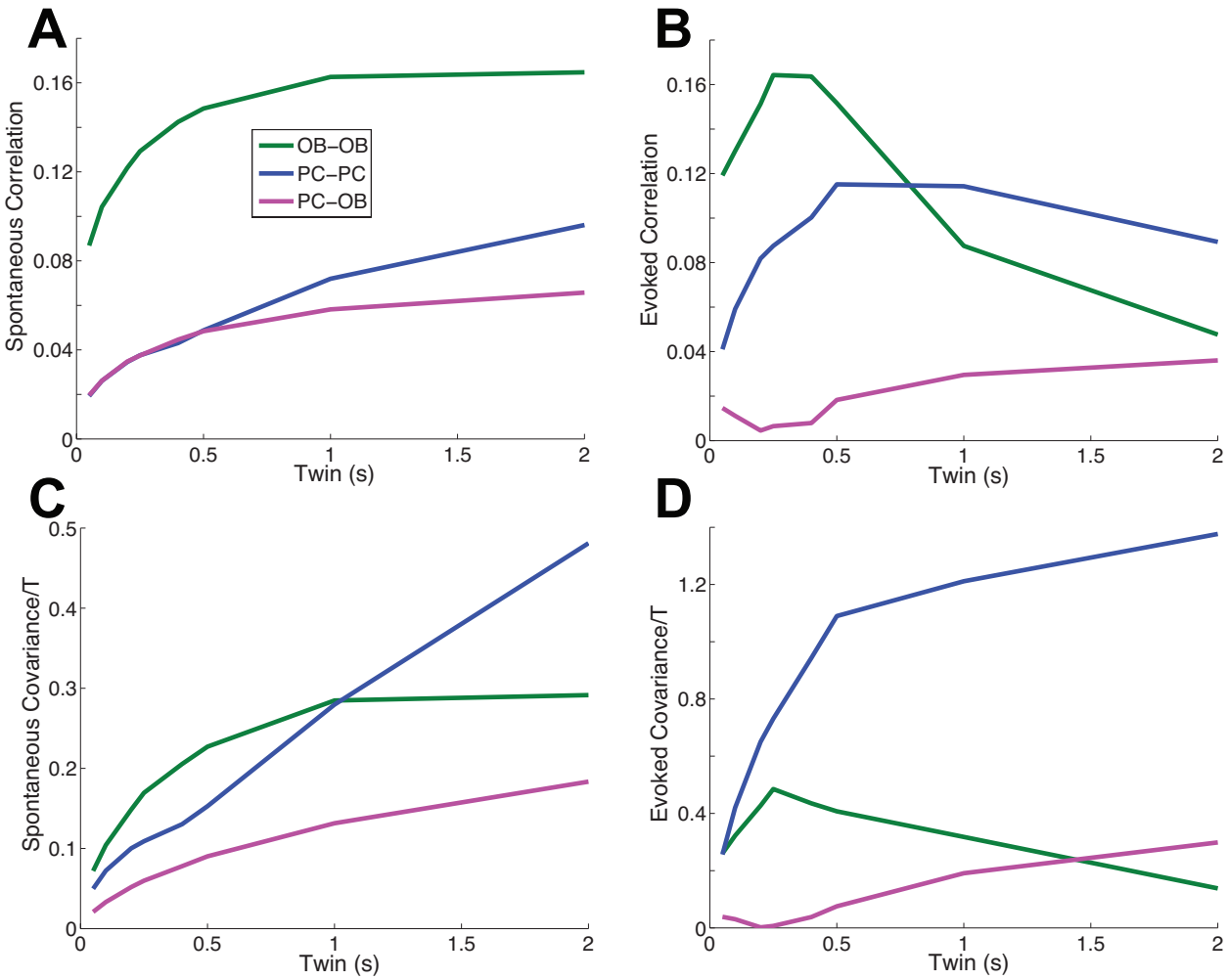

Fig S9. Cross-region correlations are smaller than within-region correlations. The experimental data shows that the PC-OB correlation and covariance is small (on average) compared to both OB and PC. A: In the spontaneous state, the (average) Fano Factor of the PC cells is larger than the OB cells. B: In the evoked state, the (average) variance of spike counts of OB cells is larger than the PC cells; here, we have divided by the time window for illustration purposes (which obviously does not change the relationship). In both A and B, there are 73 PC cells and 41 OB cells. C: In the evoked state, the (average) OB covariance is larger than the PC covariance. D: The evoked variance among OB cells is larger than the spontaneous OB variance. In C and D, the covariances were scaled by the time window for illustration purposes, and there were 1298 pairs of PC cells and 406 pairs of OB cells.

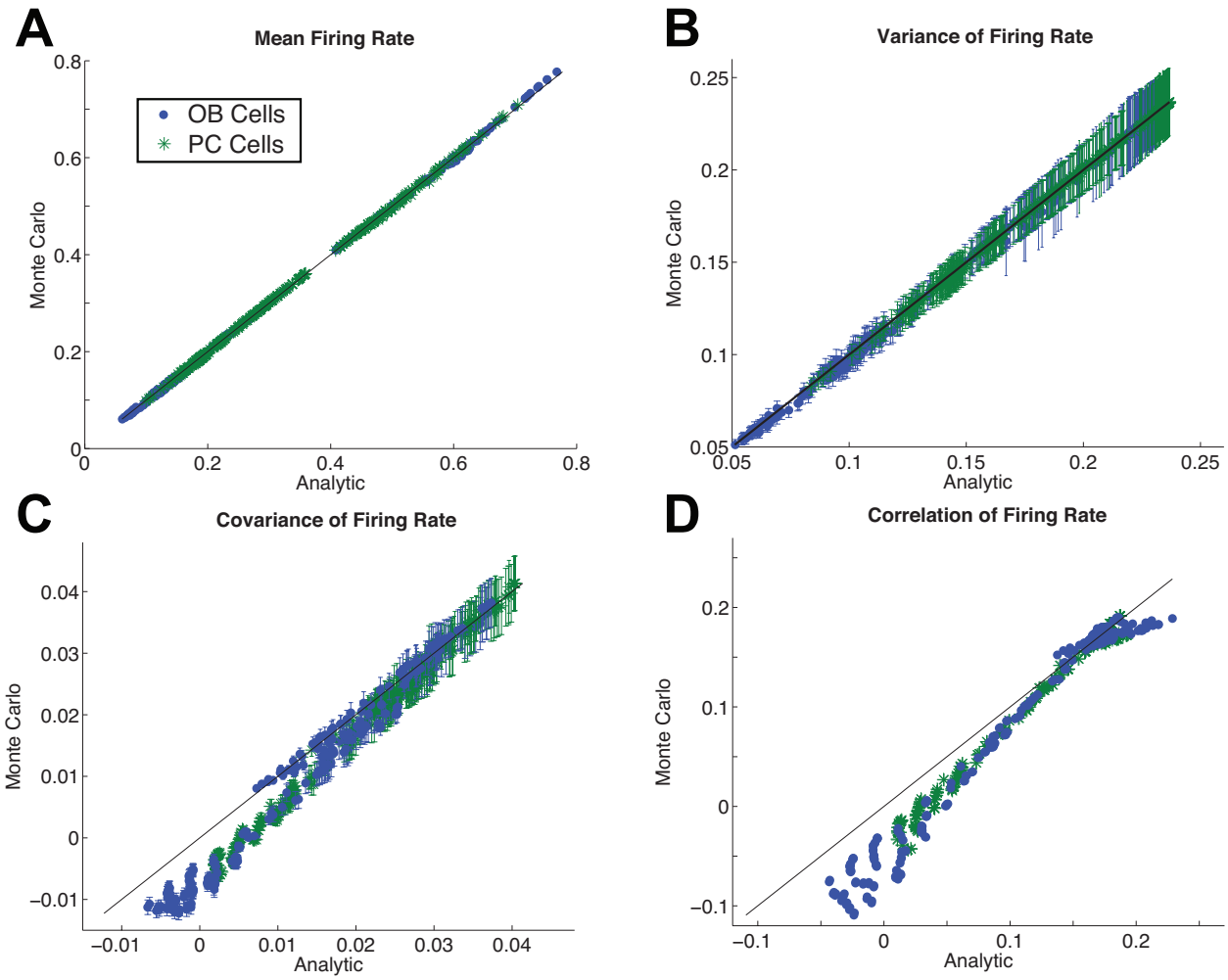

Fig S10. Fast analytic approximation accurately captures statistics of a multi-population firing rate model. Comparing the results of the fast analytic approximation to Monte Carlo simulations from 100 randomly selected parameters in the 6 equation rate model: $-2 \leq gIO < 0$, $-2 \leq gIP < 0$, $0 < gEO \leq 2$, $0 < gEP \leq 2$. Comparing 4 important firing rate statistics on a cell by cell basis (i.e., not the average across the population); the statistics for the activity X_j are just as accurate (not shown). A: The mean firing rate $F(X_j)$. B: The variance of the firing rate $Var(F(X_j))$. C: The covariance of the firing rate between OB pairs and PC pairs (we do not focus on OB–PC pairs): $Cov(F(X_j), F(X_k))$. D: The correlation of the firing rate between OB and PC pairs: $\rho = Cov(F(X_j), F(X_k))/\sqrt{Var(F(X_j))Var(F(X_k))}$. The fast analytic approximation is accurate (dots lie on the diagonal line). Error bars are shown in B and C, representing 95% confidence intervals assuming a normal distribution for finite number of realizations, or 1.96 standard deviations above and below the mean.

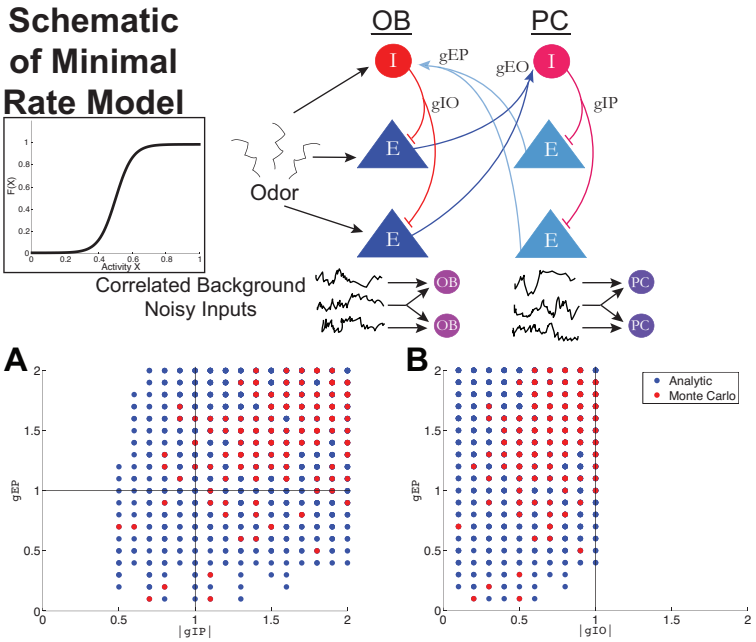

Fig S11. Experimental observations constrain conductance parameters in analytic model. The final 2 relationships between the 4 conductance parameters from the fast analytic theory for the rate model not shown in the main text with $F(X) = \frac{1}{2}(1 + \tanh((X - 0.5)/0.1))$. A: Both gEP and $|gIP|$ are relatively large. B: $|gIO|$ is relatively small.

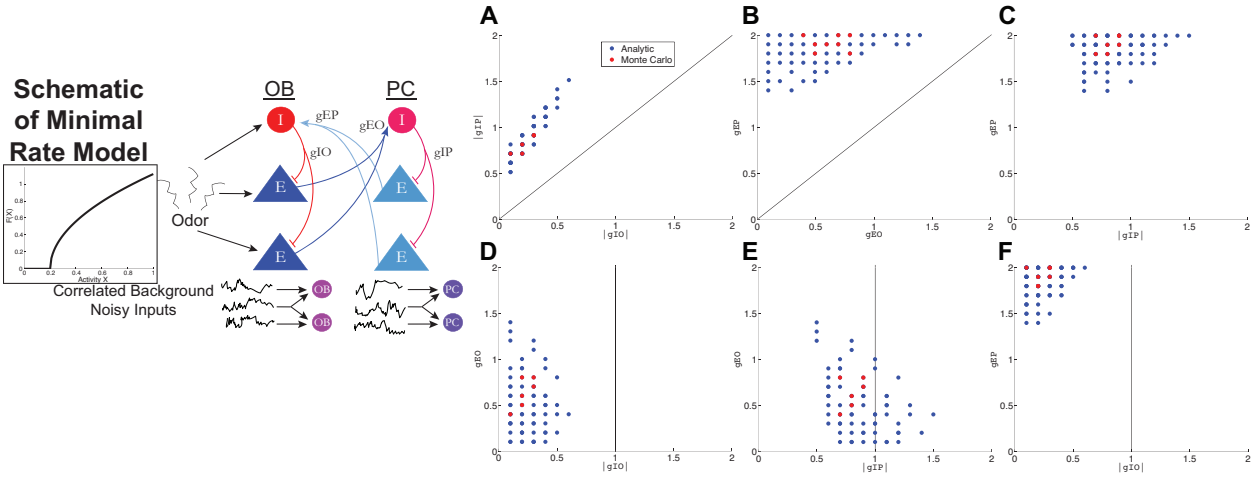

Fig S12. Analytic approximation results are robust to choice of transfer function. The results of the fast analytic theory for the rate model using a truncated square root transfer function $F(X) = 1.25\sqrt{X - 0.2}H(X - 0.2)$ are qualitatively similar to the results with the more common sigmoidal function (see main text). A: The inhibitory conductance within the PC population $|gIP|$ is larger than in the OB population gOP. B: The excitatory conductance from PC to OB gEP is generally larger than OB to PC gEO. C: Both gEP and $|gIP|$ are relatively large. D: $|gIO|$ is relatively small. E: $|gIP|$ is relatively large. F: Again, $|gIO|$ is relatively small.

Full Spiking Model, μ to PC fixed in Spon./Evoked

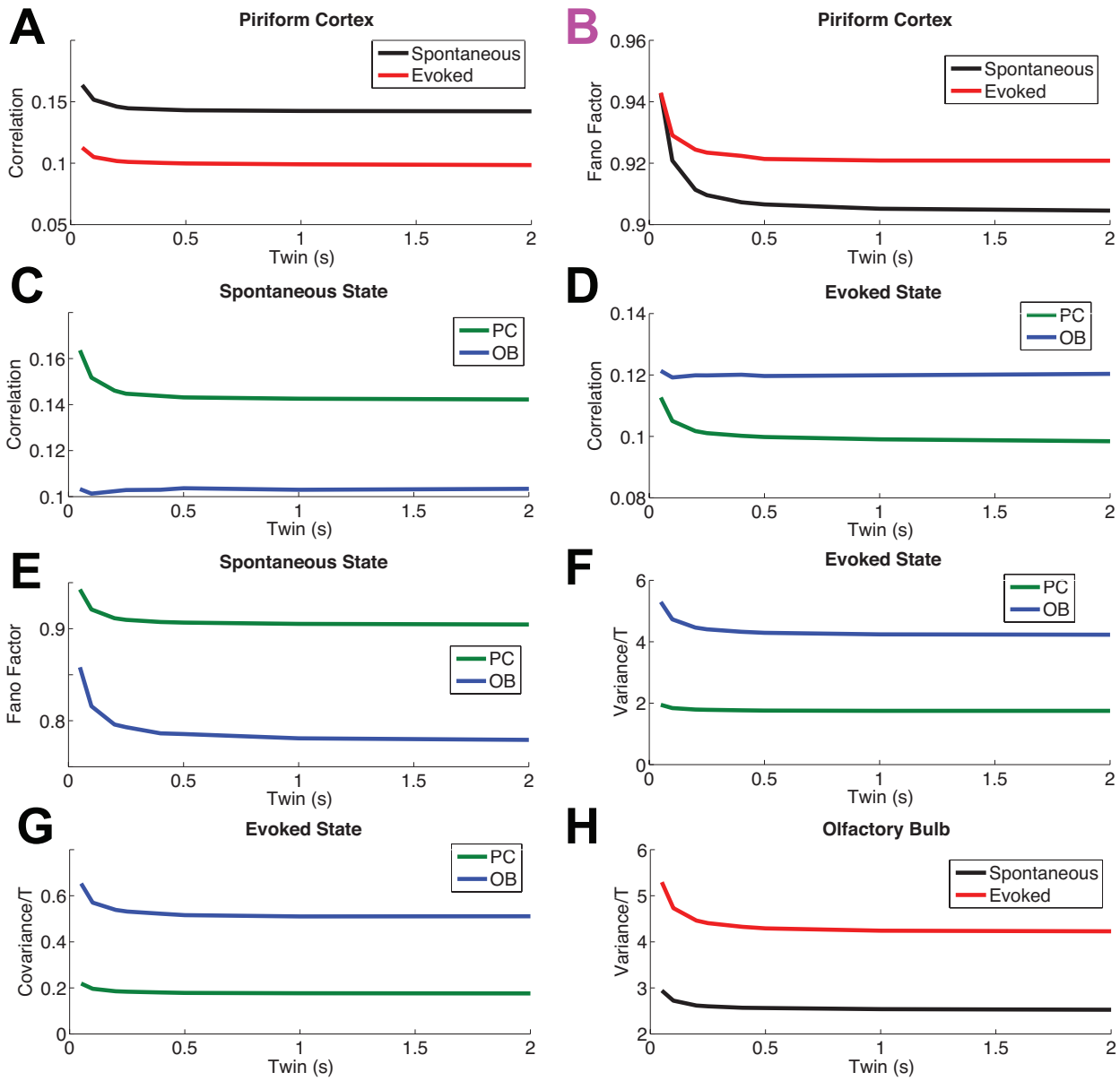

Fig S13. Mean input to PC must increase in the evoked state. Showing the results of the full LIF spiking model when the mean input to PC is the same in spontaneous and evoked states: $\mu_{PC} = 0$. The rest of the parameters are the same as in Figure 5 (see main text). The firing rates are: $\nu_{OB}^{Sp} = 3.8 \pm 3.3$, $\nu_{OB}^{Ev} = 8.6 \pm 5.4$, $\nu_{PC}^{Sp} = 2.1 \pm 2.5$, and $\nu_{PC}^{Ev} = 2.4 \pm 4.2$, which violates the constraint from the experimental data that $\nu_{OB} > \nu_{PC}$ in both states. The 8 panels show the constraints on the 2nd order spiking statistics in the same format as in Figure 5 of the main text. Only the Fano Factor constraint: $FF_{PC}^{Sp} > FF_{PC}^{Ev}$ is violated, panel B with magenta coloring.

Full Spiking Model, Test 1: gIP < gIO

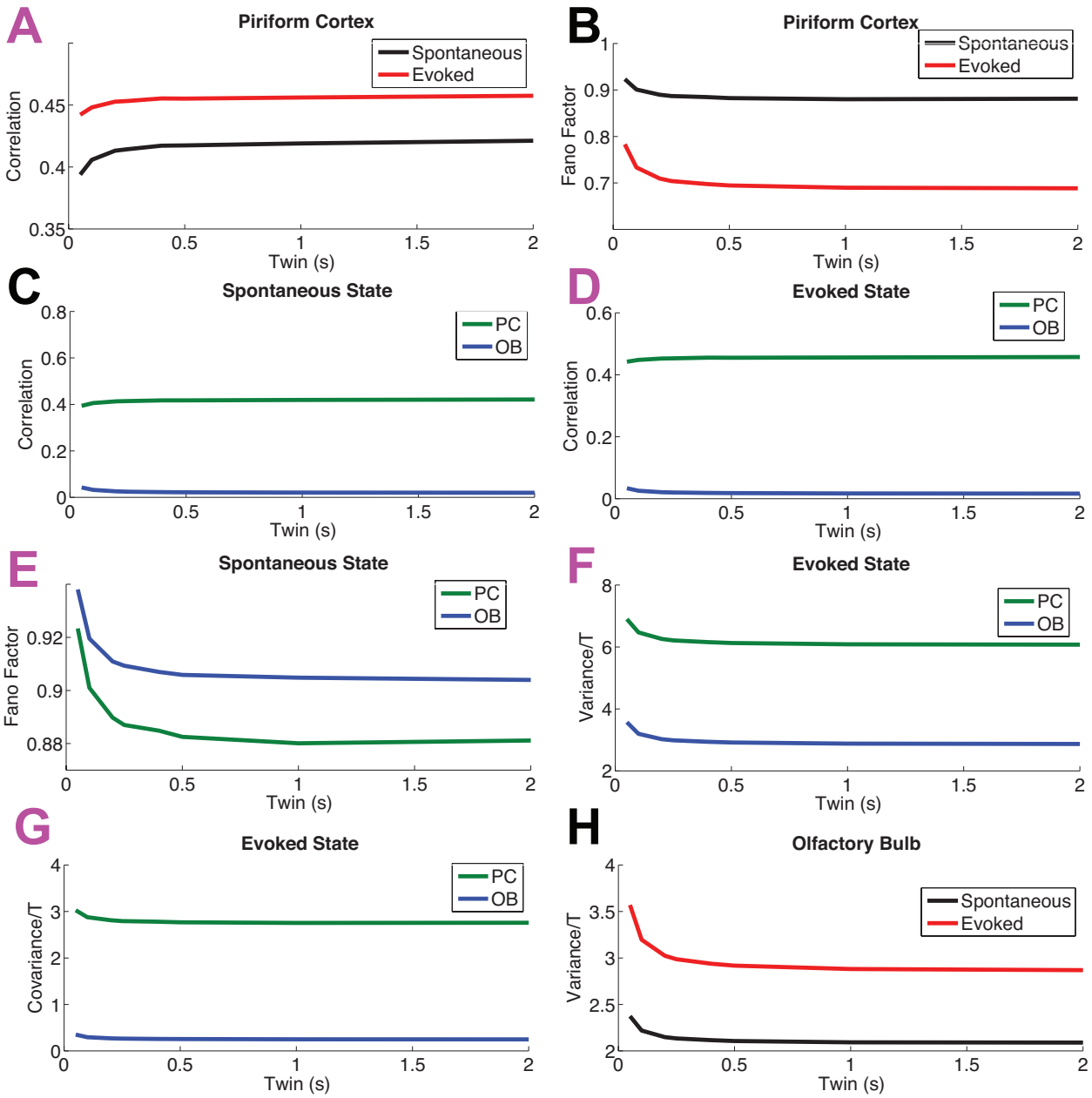

Fig S14. Violating derived relationship $|gIO| < |gIP|$ results in statistics that are inconsistent with experimental observations. Showing the results of the full LIF spiking model when $gIP < gIO$; specifically, we set $gIP = 7$ and $gIO = 20$ and set the values of the rest of the parameters to those used in Figure xxx (see main text). The firing rates are: $\nu_{OB}^{Sp} = 2.96 \pm 5$, $\nu_{OB}^{Ev} = 5.94 \pm 11.67$, $\nu_{PC}^{Sp} = 3.43 \pm 1.59$, and $\nu_{PC}^{Ev} = 8.85 \pm 3.38$, which violates the constraint from the experimental data that $\nu_{OB} > \nu_{PC}$ in both states. The 8 panels show the constraints on the 2nd order spiking statistics in the same format as in Figure xxx of the main text. The panels with magenta letters (i.e., A, D, E, F, G) are constraints that are violated.

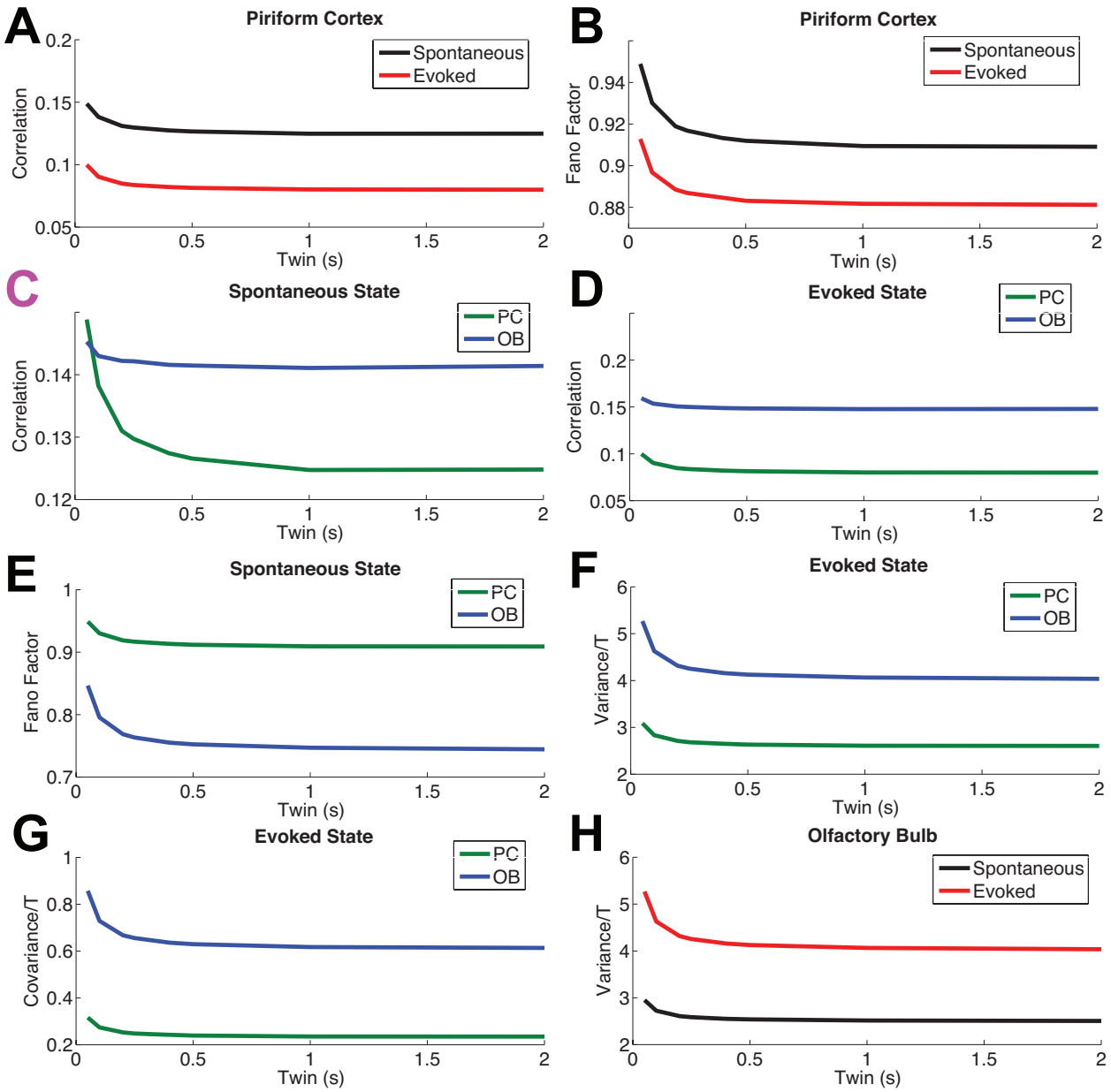

Fig S15. Violating derived relationship $gEP > gEO$ results in statistics that are inconsistent with experimental observations. Showing the results of the full LIF spiking model when $gEP < gEO$; specifically, we set $gEP = 1$ and $gEO = 15$, *and with* $\tilde{c}_{OB} = 0.6$ instead of 0.5; we set the values of the rest of the parameters to those used in Figure 5 (see main text). The firing rates are: $\nu_{OB}^{Sp} = 3.75 \pm 2.61$, $\nu_{OB}^{Ev} = 8.73 \pm 5.12$, $\nu_{PC}^{Sp} = 2.28 \pm 3.32$, and $\nu_{PC}^{Ev} = 4.87 \pm 9.2$. The 8 panels show the constraints on the 2nd order spiking statistics. Only 1 constraint is violated, panel C in magenta.

Full Spiking Model, Test 3: gIP, gEP small

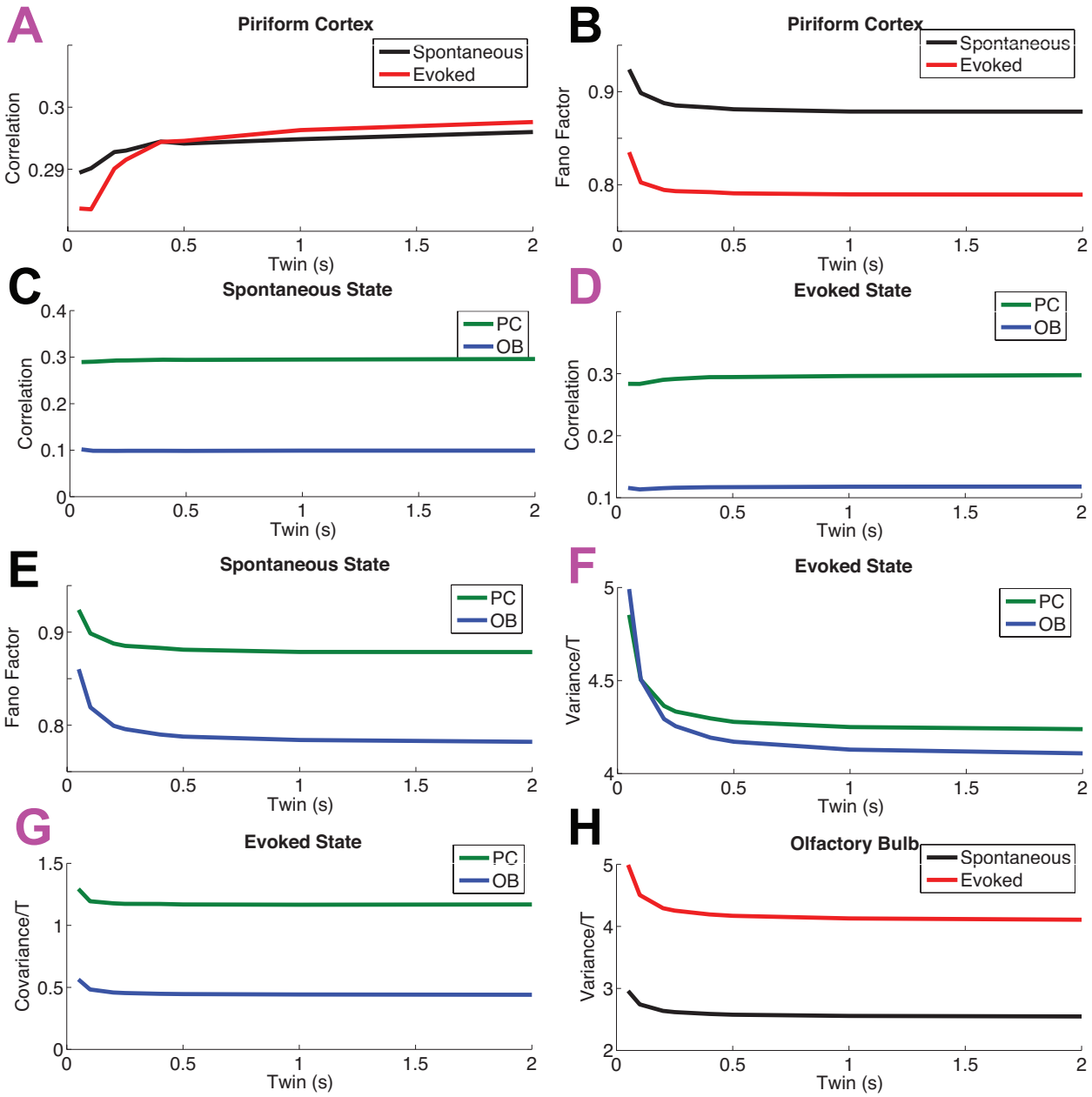

Fig S16. Violating derived relationship $gEP, gIP \gg gEO, gIO$ results in statistics that are inconsistent with experimental observations. Showing the results of the full LIF spiking model when gEP and gIP are both relatively small; specifically, we set $gEP = 10$ and $gIP = 10$ and set the values of the rest of the parameters to those used in Figure 5 (see main text). The firing rates are: $\nu_{OB}^{Sp} = 3.85 \pm 3.56$, $\nu_{OB}^{Ev} = 8.2 \pm 7.08$, $\nu_{PC}^{Sp} = 2.92 \pm 2.31$, and $\nu_{PC}^{Ev} = 6.45 \pm 6.17$, which violates the constraint from the experimental data that $\nu_{OB} > \nu_{PC}$ in both states. The 8 panels show the constraints on the 2nd order spiking statistics. The panels with magenta letters (i.e., A, D, F, G) are constraints that are violated.